Chiral Berry Plasmons in a Disk

Master's thesis

Written by *Mads A. Jørgensen*

October 17, 2017

Supervised by
Mark S. Rudner

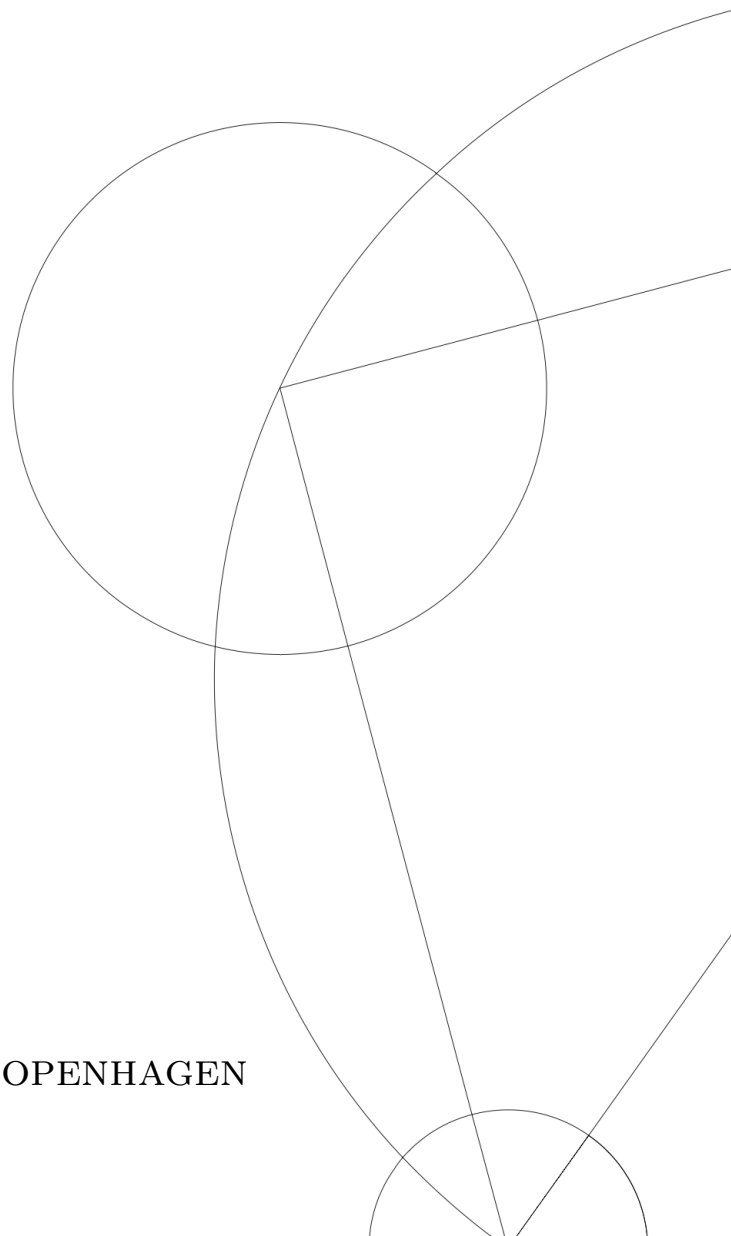

University of Copenhagen

UNIVERSITY OF COPENHAGEN

Faculty:	Faculty of Science
Institute:	University of Copenhagen; Niels Bohr Institutet
Author(s):	Mads A. Jørgensen
Email:	pmr197@alumni.ku.dk
Title and subtitle:	Chiral Berry Plasmons in a Disk -
Supervisor(s):	Mark S. Rudner
Handed in:	04.09.2017
Defended:	September 25, 2017

Name _____

Signature _____

Date _____

Abstract

Plasmons, collective excitations of free charge carriers, have manifestations in both infinite and bounded systems. The application of an external magnetic field or the use of a material exhibiting non-zero anomalous Hall conductivity allows for a chiral dispersion of the plasmon edge modes in finite systems. For this reason, they are interesting both as an object of study and for their potential application in information transmission. The system of study is that of a two-dimensional disk of charge fluid with a Hall conductance resulting from either a magnetic field or Berry curvature normal to the plane of the disk and with screening plates placed symmetrically above and below the disk-plane. A discretization scheme of modelling the disk as a set of concentric rings is used to numerically solve for the resonant modes and their associated density wave-forms. The resulting dispersions are then compared to those of the infinite half-plane. Screening has a profound effect on the electron interaction and the effect of extreme screening on the dispersions is shown. The dependence of the density wave-forms on angular momentum and excitation is briefly explored. Turning off the free carrier density, akin to setting the chemical potential in the gap of an insulator, is shown numerically to lead to one surviving unidirectional mode.

Contents

1 Introduction **4**

2 The Berry phase and Anomalous Phenomena **5**
2.1 Berry: Phase, Connection & Curvature 5
2.2 First Order Adiabatic Evolution of a State 8
2.3 Adiabatic Electron Transport Interpreted as a Result of the Berry Phase 10
2.4 Anomalous Velocity in Perturbed Crystal 11
2.5 The Quantum Anomalous Hall Effect 12
2.6 Materials Exhibiting Anomalous Phenomena 13
2.6.1 The Haldane Model and the Valley Hall Effect 14

3 Magnetoplasmons in 3-Dimensional Charge-Fluid **19**
3.1 A Toy Model for Bulk Plasmons 19
3.2 Bulk Plasmons in 3D 20
3.3 Bulk Magnetoplasmons in 3D 21
3.4 Surface Plasmons in 3D 22

4 Magnetoplasmons on a Semi-Infinite (Half-)Plane **24**

5 The Disk System **28**
5.1 The Relation Between Electrostatic Potential and Charge Density 28

6 Magnetoplasmons in a Discretized Disk **31**
6.1 On the Edge 35
6.2 Discretization of the Kernel 36
6.3 Relation to the Case of the Infinite Half-Plane 37
6.4 Results for the Magnetoplasmon - Density Profile, 3D Profile and Dispersion . . 37

7 Anomalous Berry Plasmons in Disk Geometry **40**
7.1 The system 40
7.2 Discretization of the Berry Plasmon 43
7.3 Numerical Results for the Anomalous Berry Plasmon 46
7.4 Comparison of the Exact and Approximate Kernels 48
7.5 Edge Modes in Insulator Disk 51

8 Conclusion **54**

A Edge Magnetoplasmons in Disk Geometry **55**
A.1 Analytical Eigenvalue Equation 56
A.2 Calculating the Additional Term in Equation (A.19) 58

B Auxillary plots **60**

B.1 The Splitting of Berry Modes 60

B.2 Zero-Field Wave-Forms 60

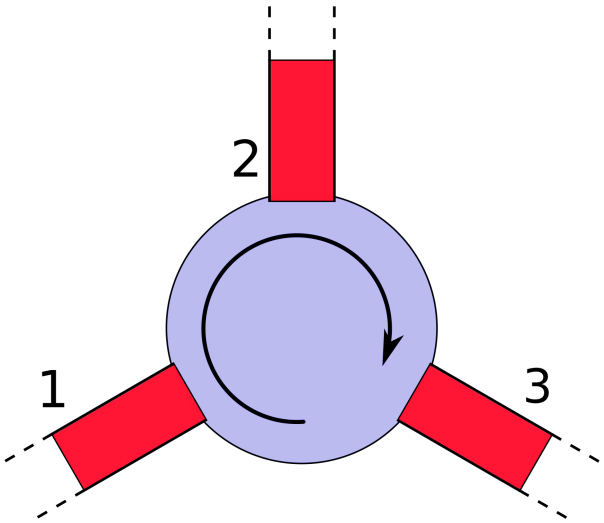

Figure 1: Schematic drawing of a simple 3-port (red) circulator with chiral signal propagation. Any signal going in through port 1 will go out through port 2, a signal going in through 2 will exit through 3 and one entering through port 3 will exit through port 1. The ports need not touch the disk; a capacitive coupling to the edge of the disk is another possibility.

1 Introduction

Throughout the past few decades, major areas of research have intertwined and helped shape the field of condensed matter physics. The discovery of topological effects and the advent of the possibility of a quantum computer have motivated the study of how to utilize the former to realize the latter. The construction of such a quantum computer poses major difficulties, among others being the problems of keeping the quantum states isolated from, or robust against, noisy suroundings and upscaling such a system to a size needed for computational purposes.
One way to help prevent accidentally destroying the quantum states is to ensure that for any data measurement made, no signal is reflected back into the system to disturb the remaining states. For this to be feasible, we need to make a device that allows for one-way signal propagation. One such contraption is known as the "circulator" [1], which consists of a disk and 3 or more ports through which signals can be emitted and absorbed. Figure 1 shows a primitive model of an ideal 3-port circulator. Any signal, for example the result of a measurement, will enter through one port, follow the edge of the disk in the one allowed direction, and enter the first port it encounters (the detector). Any reflection will then continue along the edge to the last port where it is drained out of the system, for example by grounding that port. Such a system, where reversing the starting- and end-points provides different results is called non-reciprocal. For this to happen, it is imperative that time reversal symmetry be broken somehow.

The challenge lies in devising a system that allows for this unidirectionality or, more specifically, non-recoprocity of the signal propagation. To achieve this, a capacitive coupling has been proposed[1] and utilized [2][3], where the ports are coupled to the disk through forming a capacitor, with the edge of the disk constituting one of the capacitor plates and the port

constituting the other, in such a way that there is, in addition to the coupling between port and disk, a capacitative coupling between the capacitor plates of the ports through which signals can propagate. These signals propagate with the speed of light while those propagating along the edge of the disk do so with significantly reduced velocity. Given a way to tune the velocity of signal propagation in each direction (on the disk), one can utilize this setup as an interferometer where propagation in one direction is killed while allowing it in the other.
This is where the plasmon becomes interesting. Plasmons are collective excitations of free charge carrying particles living in a rigid grid of opposite charge. When displaced from their equilibrium state the restoring force will attempt to return them to the rest state. If there is no dissipation then the particles will oscillate harmonically around the unperturbed state. When edges are present in the medium, then, as we shall see, plasmon modes that can propagate along this edge exist.
This non-recoprocity can be realized through the Hall effect which induces chirality in the modes of edge plasmons by supplying the system with an inherent direction. Traditionally, a tunable magnetic field has been used to induce this Hall effect, but the discovery of the anomalous Hall effect, resulting from the presence of a net Berry curvature, has introduced another option. It is the characteristics and workings of the anomalous Berry plasmons with which this paper will be concerned, in the hope that these plasmons will help to further the progress made in quantum computing or other unforeseen endeavours.

An outline of how the topics in this paper will progress is as follows: Firstly the Berry phase is introduced and some of its consequences are explored. Afterward we will take a look at the underlying physics of magnetoplasmons in the most approachable geometries. This is then followed by an introduction to the disk system, which is the main system of concern in this paper, and a detailed guide of the quantization scheme utilized for the numerical results shown throughout. Numerical results for magnetoplasmon phenomena on the disk are briefly considered before the main topic of anomalous Berry plasmons is approached.

2 The Berry phase and Anomalous Phenomena

This chapter will primarily follow the work of Xiao, Chang and Niu [8] and we will use mostly the same notation. In it, we will introduce the core concepts of the Berry phase, its interpretation as a result of Berry curvature, and some direct consequences of its presence.

2.1 Berry: Phase, Connection & Curvature

The concept of the Berry phase is one that appears when a quantum system undergoes an adiabatic change that causes one or more parameters to make a closed loop in their respective parameter spaces. The adiabatic theorem [9] [10] tells us that a system, described by a Hamiltonian, H, initially prepared in an eigenstate, $|n\rangle$, will stay in the instantaneous eigenstates of the system as it evolves adiabatically in time. An easily visualizable example is that of a single

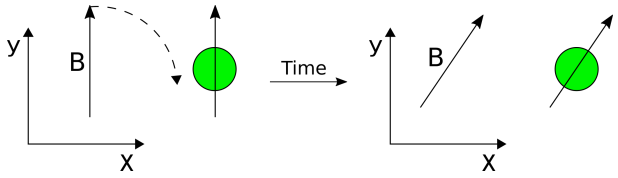

Figure 2: A classical spin aligning parallel with a magnetic field and keeping its alignment even as the magnetic field undergoes an adiabatic change.

classical spin in a magnetic field. The ground state will have the spin aligning (or anti-aligning) with the magnetic field. If the direction of this magnetic field changes slowly in time, then the eigenstate of the spin will change with it, keeping its alignment as seen in figure 2. Another example is the harmonic oscillator with slowly changing steepness of the potential, $m\omega^2 x^2$. If the change is too rapid, then we get quantum quench phenomena where suddenly an eigenstate of one Hamiltonian has to fit and be resolved by the eigenstates of another Hamiltonian.

Now, if the system and Hamiltonian depends on a set of parameters, $\mathbf{M}(t) = \{M_1(t), M_2(t), M_3(t), ...\}$, which itself depends on time, then for every time t there will be an eigenstate $|n(\mathbf{M}(t))\rangle$ such that

$$H(\mathbf{M}(t))\,|n(\mathbf{M}(t))\rangle = \epsilon_n(\mathbf{M}(t))\,|n(\mathbf{M}(t))\rangle\,. \tag{2.1}$$

The eigenstates $|n\rangle$ are not uniquely defined, however. Any arbitrary phase factor would leave equation (2.1) unaltered. As time passes, the state accumulates a dynamical phase factor proportional to temporal integral of the eigenenergy. We will also allow it to have a second time-dependent (and band-dependent) phase, $\gamma_n(t)$. This means that the full state at a given time, t, is

$$|\psi_n(t)\rangle = \mathrm{e}^{i\gamma_n(t)} \exp\left(-\frac{i}{\hbar}\int_0^t dt' \epsilon_n(\mathbf{M}(t'))\right) |n(\mathbf{M(t)})\rangle\,. \tag{2.2}$$

From here the Schrödinger equation,

$$i\hbar\frac{\partial}{\partial t}\,|\psi_n(t)\rangle = H(\mathbf{M}(t))\,|\psi_n(t)\rangle\,, \tag{2.3}$$

will give us an expression for the time evolution of the additional phase, $\gamma_n(t)$. The LHS gives

$$i\hbar\frac{\partial}{\partial t}\,|\psi_n(t)\rangle = (-\hbar\dot{\gamma}_n + \epsilon_n(t))\,|\psi_n(t)\rangle + i\hbar\mathrm{e}^{i\gamma_n(t)} \exp\left(-\frac{i}{\hbar}\int_0^t dt' \epsilon_n(\mathbf{M}(t'))\right) \frac{\partial \mathbf{M}(t)}{\partial t}\cdot\frac{\partial}{\partial \mathbf{M}}\,|n(\mathbf{M})\rangle\,. \tag{2.4}$$

The RHS just gives us the eigenenergy,

$$H(\mathbf{M}(t))\,|\psi_n(t)\rangle = \epsilon_n(\mathbf{M}(t))\,|\psi_n(t)\rangle\,. \tag{2.5}$$

Equating the two, multiplying by $\langle\psi|$ from the left and cancelling the $\epsilon_n\,|\psi\rangle$ terms and factors of $\hbar$ leaves us with

$$\begin{aligned} \dot{\gamma}_n &= i \langle n| \frac{\partial \mathbf{M}(t)}{\partial t} \cdot \frac{\partial}{\partial \mathbf{M}} |n\rangle \Leftrightarrow \\ \gamma_n &= i \int_{t_i}^{t_f} dt \langle n| \frac{\partial \mathbf{M(t)}}{\partial t} \cdot \frac{\partial}{\partial \mathbf{M}} |n\rangle = i \int_{\mathbf{M}(t_i)}^{\mathbf{M}(t_f)} d\mathbf{M} \cdot \langle n| \frac{\partial}{\partial \mathbf{M}} |n\rangle . \end{aligned} \tag{2.6}$$

Equation (2.6) is often written in terms of the Berry vector potential, similar to that used in electromagnetism, or the Berry connection, analogous to connections from differential geometry and used in general relativity,

$$\gamma_n = \int_{\mathbf{M}(t_i)}^{\mathbf{M}(t_f)} d\mathbf{M} \cdot \mathcal{A}_n(\mathbf{M}), \tag{2.7}$$

where the Berry connection (which shall be the nomenclature used throughout this thesis) is given by

$$\mathcal{A}_n(\mathbf{M}) = i \langle n(\mathbf{M})| \frac{\partial}{\partial \mathbf{M}} |n(\mathbf{M})\rangle . \tag{2.8}$$

Just like the electromagnetic vector potential, the Berry connection is gauge dependent; Changing the eigenstates by an overall $\mathbf{M}$-dependent phase, $|n\rangle \rightarrow \mathrm{e}^{i\phi(\mathbf{M})} |n\rangle$, changes the Berry connection by an extra term,

$$\mathcal{A}_n \rightarrow \mathcal{A}_n - \frac{\partial \phi(\mathbf{M})}{\partial \mathbf{M}}. \tag{2.9}$$

Inserting equation (2.9) into equation (2.7) shows that the Berry phase will then be changed by an additional term of (let $t_i = 0$)

$$\gamma_n \rightarrow \gamma_n - [\phi(\mathbf{M}(t_f)) - \phi(\mathbf{M}(0))] . \tag{2.10}$$

When $\phi(\mathbf{M}(0)) - \phi(\mathbf{M}(t_f))$ is non-zero we can make a choice of gauge that causes this additional term to cancel with the original Berry phase. If the phase is single-valued in $\mathbf{M}$ (as it will if the parameter space is simply connected) then this is not possible when $\mathbf{M}(t_f) = \mathbf{M}(0)$, i.e. when traversing a closed loop in parameter space, which then means that

$$\phi(\mathbf{M}(0)) - \phi(\mathbf{M}(t_f)) = 0, \tag{2.11}$$

where c is an integer.
We can now write the "physical part" of the Berry Phase as

$$\gamma_n = i \oint_d \mathbf{M} \cdot \mathcal{A}_n(\mathbf{M}). \tag{2.12}$$

Also similarly to electromagnetism, we can define a tensor in parallel to the force tensor,

$$\Omega_{\mu\nu}(\mathbf{M}) = \frac{\partial}{\partial M^\mu} \mathcal{A}_\nu(\mathbf{M}) - \frac{\partial}{\partial M^\nu} \mathcal{A}_\mu(\mathbf{M}) = i \left[\langle \frac{\partial n(\mathbf{M})}{\partial M^\mu} | \frac{\partial n(\mathbf{M})}{\partial M^\nu} \rangle - \langle \frac{\partial n(\mathbf{M})}{\partial M^\nu} | \frac{\partial n(\mathbf{M})}{\partial M^\mu} \rangle \right], \tag{2.13}$$

called the Berry curvature. Here we have suppressed the band index, n. For three-dimensional parameter spaces equation (2.13) reduces to a regular curl,

$$\mathbf{\Omega}(\mathbf{M}) = \nabla_{\mathbf{M}} \times \mathcal{A}(\mathbf{M}). \tag{2.14}$$

The Berry curvature is, much like the electric and magnetic fields it mirrors, gauge independent, which can be seen from either the above expression or equation (2.13).

A rewriting of equation (2.13) can be done to shift the differentiations from the eigenstate vectors to the Hamiltonian of the system, which is often advantageous when there could be ambiguity regarding the relative phase of the eigenstates. One case with such an ambiguity could be when doing numerical computations where one risks the eigenvectors having different phases.

For this rewriting we first note that for two different (orthonormal) eigenstates of the Hamiltonian, $|n\rangle$ and $|n'\rangle$ with $n \neq n'$, we have

$$\frac{\partial}{\partial M}\left(\langle n| H |n'\rangle\right) = \langle \frac{\partial n}{\partial M}|n'\rangle \, \epsilon_{n'} + \langle n| \frac{\partial H}{\partial M} |n'\rangle + \langle n|\frac{\partial n'}{\partial M}\rangle \, \epsilon_n = 0, \tag{2.15}$$

where the last equality comes from the orthogonality of the eigenstates. From here we can partially integrate the last term,

$$\langle n|\frac{\partial n'}{\partial M}\rangle = \frac{\partial}{\partial M}\left(\langle n|n'\rangle\right) - \langle \frac{\partial n}{\partial M}|n'\rangle = -\langle \frac{\partial n}{\partial M}|n'\rangle \tag{2.16}$$

and use that to rewrite equation (2.15) to

$$\langle \frac{\partial n}{\partial M}|n'\rangle = \frac{1}{\epsilon_n - \epsilon_{n'}} \langle n| \frac{\partial H}{\partial M} |n'\rangle \, . \tag{2.17}$$

Finally, using equation (2.17) we can rewrite equation (2.13) to

$$\Omega^n_{\mu\nu} = i \sum_{n' \neq n} \frac{1}{(\epsilon_n - \epsilon_{n'})^2} \left[\langle n| \frac{\partial H}{\partial M^\mu} |n'\rangle \langle n'| \frac{\partial H}{\partial M^\nu} |n\rangle - \langle n| \frac{\partial H}{\partial M^\nu} |n'\rangle \langle n'| \frac{\partial H}{\partial M^\mu} |n\rangle \right], \tag{2.18}$$

where we have reintroduced the band index, and the summation is over $n \neq n'$ because the $n' = n$ term dies (as already evident when inserting a complete set of basis states in equation (2.13) and noting that equation (2.16) works even for $n' = n$). Furthermore, equation (2.18) shows that the total sum of the Berry curvature of all bands cancels, $\sum_n \Omega^n_{\mu\nu} = 0$.

2.2 First Order Adiabatic Evolution of a State

In this chapter we will, following the lead of the appendix of [8], attempt to shed some light on how a quantum state evolves in time when the Hamiltonian (the system), which depends on a set of parameters, changes adiabatically in time. The result will be tied together with the concept of the Berry curvature to show how it can affect the movement of charged particles.

The evolution of a state $|\psi\rangle$ is governed by the Schrödinger equation (see equation (2.3)). We can write $|\psi\rangle$ as a sum of eigenstates of the hamiltonian, $|l\rangle$, each with energy E_l,

$$\psi(t) = \sum_l \exp\left[-\frac{i}{\hbar}\int_{t_0}^{t} dt' E_l(t')\right] a_l(t)\,|l(t)\rangle\,. \tag{2.19}$$

Inserting this into the Schrödinger equation and mutiplying $\langle n|$ from the left gives a differential equation for the time evolution of the expansion coefficients, a_l,

$$\frac{d}{dt}a_n = -\sum_l a_l\,\langle n|\,\frac{\partial}{\partial t}\,|l\rangle \exp\left(-\frac{i}{\hbar}\int_{t_0}^{t} dt'[E_l(t') - E_n(t')]\right). \tag{2.20}$$

Just like previously mentioned, these eigenstates of the Hamiltonian could have an additional phase factor. Instead of requiring this phase to be single-valued we will instead require the eigenstates to fulfill the parallel transport condition,

$$\langle n(\mathbf{M}(t))|\,\frac{\partial}{\partial t}\,|n(\mathbf{M}(t))\rangle = \dot{\mathbf{M}}(t)\,\langle n|\,\frac{\partial}{\partial \mathbf{M}}\,|n\rangle = 0, \tag{2.21}$$

which ensures that the change in each eigenstate is orthogonal to the eigenstate itself. Any global (non-physical, arbitrary) time-dependent phase that we might add to the eigenstates will stay "constant" between two temporally close states, $\langle n(t)|n(t+\delta t)\rangle \approx 1$, as can be seen by letting $|n\rangle \to \mathrm{e}^{i\theta(t)}\,|n\rangle$ in equation (2.21). This leads to $\frac{d}{dt}\theta(t) = 0$.
The states that fulfill equation (2.21) we call $|\tilde{n}\rangle$. After a trip through different values of $\mathbf{M}(t)$ the state $|\tilde{n}\rangle$ will have acquired a phase. If $\mathbf{M}(t_f) = \mathbf{M}(t_0)$ then the acquired phase is the Berry phase, $|\tilde{n}(t_f)\rangle = \mathrm{e}^{i\gamma_n}\,|\tilde{n}(t_0)\rangle$.

For adiabatic change we are in the limit $\dot{\mathbf{M}} \to 0$ which means that $\frac{d}{dt}a_n \approx 0$. For small, but non-zero, $\dot{\mathbf{M}}$ we can prepare our system in an eigenstate, $|n\rangle$, at time $t = 0$, such that $a_n(0) = 1$ and $a_{n'\neq n}(0) = 0$. According to equations (2.20)-(2.21) we have $\dot{a}_n = 0$ (the $l = n$ term in equation (2.20) is killed off by the parallel transport requirement) and, for $n' \neq n$ the only contribution we get from the sum comes from the $l = n$ term,

$$\frac{d}{dt}a_{n'} = -\,\langle \tilde{n}'|\,\frac{\partial}{\partial t}\,|\tilde{n}\rangle \exp\left(-\frac{i}{\hbar}\int_{t_0}^{t} dt'[E_n(t') - E_{n'}(t')]\right). \tag{2.22}$$

In the adiabatic limit the non-exponential factor changes slowly compared to the oscillation of the phase factor. Likewise, the energy difference, $E_n - E_{n'}$ is much larger than the change in the energies, and so the solution can be written as

$$a_{n'} = -i\hbar\frac{\langle \tilde{n}'|\,\frac{\partial}{\partial t}\,|\tilde{n}\rangle}{E_n(t) - E_{n'}(t)} \exp\left(-\frac{i}{\hbar}\int_{t_0}^{t} dt'[E_n(t') - E_{n'}(t')]\right). \tag{2.23}$$

Differentiating the solution w.r.t. time and killing terms proportional to $\frac{d}{dt}(\langle \tilde{n}'|\,\frac{\partial}{\partial t}\,|\tilde{n}\rangle)$ and $\frac{1}{(E_n(t)-E_{n'}(t))^2}$ returns equation (2.22). This means that the first order time evolution of the state $|\psi\rangle$, initially prepared in the state $|\tilde{n}\rangle$, is given by

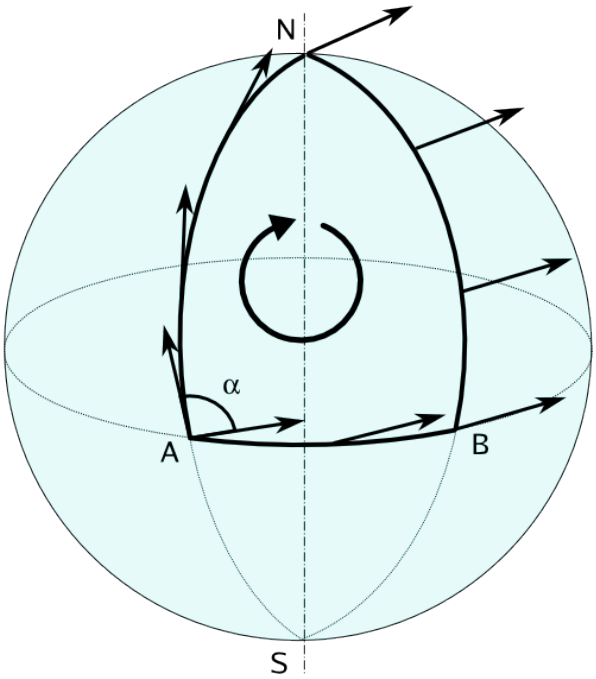

Figure 3: Visualization of the phase accumulation of a state after undergoing an adiabatic loop in a curved parameter space. Picture taken from https:en.wikipedia.org/wiki/Parallel_transport, created by user Fred the Oyster.

$$\begin{aligned} |\psi(t)\rangle &= \sum_l \exp\left(-\frac{i}{\hbar}\int_{t_0}^{t} dt' E_l(t')\right)\left(a_l^{0^{th}order} + a_l^{1^{st}order}\right)|\tilde{l}(t)\rangle \\ &= \exp\left(-\frac{i}{\hbar}\int_{t_0}^{t} dt' E_n(t')\right)\left[|\tilde{n}(t)\rangle + i\hbar\sum_{n'\neq n}\frac{\langle\tilde{n}'|\frac{\partial}{\partial t}|\tilde{n}\rangle}{E_n(t)-E_{n'}(t)}|\tilde{n}'(t)\rangle\right]. \end{aligned} \tag{2.24}$$

This result will be used in the next chapter to show the implications of the presence of Berry curvature.

2.3 Adiabatic Electron Transport Interpreted as a Result of the Berry Phase

We can use equation (2.24) to get a picture of how electrons move in a crystal exposed to a Hamiltonian that changes cyclically and adiabatically in time. We imagine a one-dimensional insulator (for simplicity) governed by a Hamiltonian, $H(q,t) = H(q,t+T)$, where T is one period of the cycle, with regular bloch eigenstates, $\mathrm{e}^{iqx}|u_n(q,t)\rangle$, and eigenenergies ϵ_n. These states will, when initially prepared in the n'th state and to first order in the time evolution, be (here we have omitted the phase; it will cancel for our results in the end)

$$|\psi(t)\rangle \approx |u_n(t)\rangle - i\hbar\sum_{n\neq n'}\frac{\langle u_{n'}|\frac{\partial}{\partial t}|u_n\rangle}{\epsilon_n-\epsilon_{n'}}|u_{n'}(t)\rangle\,. \tag{2.25}$$

The expectation value of the velocity operator, as given by Hamilton's equations, $v_n(q,t) = \frac{\partial H}{\hbar\partial q}$, is then, to first order

$$\begin{aligned}\langle v_n(q,t)\rangle &= \langle\psi(t)|\frac{\partial H}{\hbar\partial q}|\psi(t)\rangle \\ &= \frac{\partial\epsilon_n}{\hbar\partial q} - i\sum_{n'\neq n}\left[\langle u_n|\frac{\partial H}{\partial q}|u_{n'}\rangle\,\frac{\langle u_{n'}|\frac{\partial u_n}{\partial t}\rangle}{\epsilon_n-\epsilon_{n'}} - \frac{\langle\frac{\partial u_n}{\partial t}|u_{n'}\rangle}{\epsilon_n-\epsilon_{n'}}\,\langle u_{n'}|\,\frac{\partial H}{\partial q}\,|u_n\rangle\right].\end{aligned} \tag{2.26}$$

This can be rewritten to something more palatable by using equations (2.16) and (2.17) and the fact that the eigenstates, $|u_n\rangle$, make up a complete set, $\sum_n |u_n\rangle\langle u_n| = \mathbb{1}$,

$$\begin{aligned}\langle v_n(q,t)\rangle &= \frac{\partial\epsilon_n}{\hbar\partial q} - i\sum_{n'\neq n}\left[\left(\frac{\partial}{\partial q}\langle u_n|\right)|u_{n'}\rangle\langle u_{n'}|\frac{\partial}{\partial t}|u_n\rangle - \left(\frac{\partial}{\partial t}\langle u_n|\right)|u_{n'}\rangle\langle u_{n'}|\frac{\partial}{\partial q}|u_n\rangle\right] \\ &= \frac{\partial\epsilon_n}{\hbar\partial q} - i\left[\langle\frac{\partial u_n}{\partial q}|\frac{\partial u_n}{\partial t}\rangle - \langle\frac{\partial u_n}{\partial t}|\frac{\partial u_n}{\partial q}\rangle\right].\end{aligned} \tag{2.27}$$

The last term is just what appears in equation (2.13), and so we can finally simplify to

$$\langle v_n(q,t)\rangle = \frac{\partial\epsilon_n}{\hbar\partial q} - \Omega^n_{qt}, \tag{2.28}$$

which gives us the first taste of the physically observable nature of Berry phenomena.

2.4 Anomalous Velocity in Perturbed Crystal

Finally, for our purposes we will want to examine the situation in which we have an induced electric field due to an excitation of a plasmon in a material with non-zero Berry curvature.

Imagine a crystal where we apply a weak uniform electric field through a time dependent vector potential (remember that $\mathbf{E} = -\nabla\phi - \frac{\partial\mathbf{A}}{\partial t}$), such that it does not break the discrete translational invariance of our hamiltonian. The perturbation enters the hamiltonian in the usual way and we get

$$H(t) = \frac{(\hat{p} + e\mathbf{A}(t))^2}{2m} + V(\mathbf{r}). \tag{2.29}$$

We can make a unitary transformation on this Hamiltonian to bring it to the form of a Bloch Hamiltonian,

$$\tilde{H} = \mathrm{e}^{i\frac{e}{\hbar}\mathbf{A}\cdot\mathbf{r}} H \mathrm{e}^{-i\frac{e}{\hbar}\mathbf{A}\cdot\mathbf{r}} = \frac{\hat{p}^2}{2m} + V(\mathbf{r}). \tag{2.30}$$

This hamiltonian just has the usual Bloch eigenstates,

$$|\psi_n(t)\rangle = \mathrm{e}^{i\mathbf{q}\cdot\mathbf{r}}\,|u_n(t)\rangle\,. \tag{2.31}$$

In momentum space it has the usual Bloch eigenenergies

$$\tilde{H}(\mathbf{q},t)\,|\psi_n(\mathbf{q},t)\rangle = \epsilon_n(\mathbf{q})\,|\psi_n(\mathbf{q},t)\rangle\,, \tag{2.32}$$

so that

$$\langle\psi_n(t)|\tilde{H}|\psi_n(t)\rangle = \langle u_n(t)|\mathrm{e}^{-i\left(\mathbf{q}-\frac{e}{\hbar}\mathbf{A}\right)\cdot\mathbf{r}}H(\mathbf{q})\mathrm{e}^{i\left(\mathbf{q}-\frac{e}{\hbar}\mathbf{A}\right)\cdot\mathbf{r}}|u_n(t)\rangle = \epsilon_n(\mathbf{q},t), \tag{2.33}$$

where we have suppressed that the vector potential is time-dependent (and linear in time for a uniform electric field). Making a change of variables, $\mathbf{q}' = \mathbf{q} - \frac{e}{\hbar}\mathbf{A}$ and renaming $\mathbf{q}' \to \mathbf{q}$ gives us a Hamiltonian, $H(q,t)$, that depends only on the term $\mathbf{q} + \frac{e}{\hbar}\mathbf{A}(t) \equiv \mathbf{k}$ with eigenenergies $\epsilon_n(\mathbf{q} + \frac{e}{\hbar}\mathbf{A}(t)) = \epsilon_n(\mathbf{k})$.

The temporal derivative of the new crystal momentum is

$$\dot{\mathbf{k}} = -\frac{e}{\hbar}\mathbf{E} \tag{2.34}$$

Using the chain rule on $\frac{\partial}{\partial t}|u_n(\mathbf{k})\rangle$ we get from equation (2.34) that

$$\frac{\partial}{\partial t} = -\frac{e}{\hbar}E_j\frac{\partial}{\partial k_j}, \tag{2.35}$$

where we sum over the repeated indices, and this, combined with the observation that $\frac{\partial}{\partial k_j} = \frac{\partial}{\partial q_j}$, leads to the fact that equation (2.27) for a 3-dimensional system (recall that this was for a one-dimensional system; each component of a three-dimensional system can be treated like (2.27)) can be rewritten to the form

$$\mathbf{v}_n(\mathbf{k}) = \frac{\partial\epsilon_n(\mathbf{k})}{\hbar\partial\mathbf{k}} - \frac{e}{\hbar}\mathbf{E}\times\mathbf{\Omega}_\mathbf{n}(\mathbf{k}), \tag{2.36}$$

where

$$\mathbf{\Omega}_n(\mathbf{k}) = i\left\langle\nabla_\mathbf{k}u_n\right|\times\left|\nabla_\mathbf{k}u_n\right\rangle. \tag{2.37}$$

What we see here is that an electric field applied to a crystal with non-zero Berry curvature causes the appearance of a velocity component transverse to the electric field. An analogy can be made to the Hall effect where a similar transverse velocity is induced by a magnetic field rather than a Berry curvature. The Hall effect caused by a Berry curvature is called the Anomalous Hall Effect.

Equation (2.36) also completes the "symmetry" of the time evolution of the position and momentum coordinates of a charged particle in an electromagnetic field by providing a counterpart to the Lorentz force, where $\dot{p}$ has a term proportional to $\mathbf{v}\times\mathbf{B}$.

2.5 The Quantum Anomalous Hall Effect

Equation (2.36) tells us that an electric field will cause a transverse current to flow, and from that thought it is not far fetched to expect a Hall-like effect. The current is proportional to the average of the velocity of all the filled states,

$$\mathbf{j} = -e\sum_n\int_{\mathrm{BZ}}\frac{d^2k}{(2\pi)^2}f_n(\mathbf{k})\mathbf{v}_n(\mathbf{k}) = -e\int_{\mathrm{BZ}}\frac{d^2k}{(2\pi)^2}f_n(\mathbf{k})\left[\frac{\partial\epsilon_n(\mathbf{k})}{\hbar\partial\mathbf{k}} - \frac{e}{\hbar}\mathbf{E}\times\mathbf{\Omega}_\mathbf{n}(\mathbf{k})\right], \tag{2.38}$$

where f_n is a filling function. For an insulator these states correspond to the filled valence band, so that $f_{\text{val}}(\mathbf{k}) = 1$ for the valence band and $f_{\text{con}}(\mathbf{k}) = 0$ for the conduction band. Let us examine the transverse conductivity for the simple case of an insulator (with only one valence and conductance band) with a constant electric field in the y-direction, $\mathbf{E} = E_y\hat{y}$. The insulator has a net Berry curvature pointing in the z-direction, $\mathbf{\Omega}(\mathbf{k}) = \Omega(\mathbf{k})\hat{z}$. The periodicity (in crystal momentum) of the valence band makes the integral of the first term over the entire Brillouin zone vanish. In this case there will only be one component of the current that survives, namely the x-component, because of the cross product.
What we are left with is

$$j_x = \frac{e^2}{\hbar}\int_{\text{BZ}} \frac{d^2k}{(2\pi)^2}\Omega(\mathbf{k})E_y, \tag{2.39}$$

which means, from $j_i = \sigma_{ij}E_j$, that the transverse conductivity is given by

$$\sigma_{xy} = \frac{e^2}{h}\int_{\text{BZ}} \frac{d^2k}{2\pi}\Omega(\mathbf{k}) \equiv \frac{e^2}{h}c, \tag{2.40}$$

where $c = \int_{\text{BZ}} \frac{d^2k}{2\pi}\Omega(\mathbf{k})$ is an integer called the Chern number. This quantity has been shown to be inherent to the topology of the system, and therefore impervious to continuous deformations of the system, only changeable by a discrete deformation, such as closing of an energy gap [15]. If the system is not an insulator, but rather a conductor with a partially filled conductance band, then the integration over all k-values should include these states which will result in a different, non-integer, contribution to the Hall conductivity.

2.6 Materials Exhibiting Anomalous Phenomena

For a crystal to have non-vanishing Berry curvature it must have broken either time reversal symmetry or inversion symmetry. This can be seen by applying the symmetry considerations to equation (2.36) and noting that velocity, $\mathbf{v}$, and crystal momentum, $\mathbf{k}$, both change sign under either either inversion, while the electric field is unchanged by time reversal but changes sign under spatial inversion. Time reversal symmetry can be broken by the presence of a magnetic field, either intrinsic or external. Alternatively, a gap can be induced by a broken spatial inversion symmetry. This can be achieved through strong spin-orbit interaction (SOI) or by having an A-B lattice, where nearest neighbouring atoms are different. An example of a system with strong SOI is the HgTe-CdTe quantum well structure[14] and an example of one such lattice is hexagonal Boron-Nitride, hBN. This has the hexagonal honeycomb lattice structure of graphene (which has the characteristic Dirac cones with massless fermion states), but with two different atoms in the unit cell. With identical atoms (like graphene) the on-site energy of the atoms contribute only a constant to the (linearized around $k = 0$, centered on a Dirac point) 2×2 Hamiltonian (in a "site-spinor" formalism) and we are left with off-diagonal hopping terms so that the Hamiltonian can be written as a parameterized "magnetic" Hamiltonian,

$$H(\mathbf{k}) \propto \mathbf{D}(\mathbf{k}) \cdot \sigma, \tag{2.41}$$

where $\mathbf{D}(\mathbf{k})$ is a vector with $D_z = 0$ and σ is the "vector" of Pauli matrices,

$$\begin{aligned} \sigma_x &= \begin{pmatrix} 0 & 1 \\ 1 & 0 \end{pmatrix} \\ \sigma_y &= \begin{pmatrix} 0 & -i \\ i & 0 \end{pmatrix} \\ \sigma_z &= \begin{pmatrix} 1 & 0 \\ 0 & -1 \end{pmatrix}. \end{aligned} \tag{2.42}$$

Hamiltonians on the form of that of equation (2.41) are called Bloch Hamiltonians and in section 2.6.1 we will explore more in depth how such a Hamiltonian can arise. The eigenstates will align along the vector $\mathbf{D}$, which acts as a "magnetic field". Translating this in-plane magnetic field to the Bloch sphere, we see that this limits the states to lie in the plane of equiprobable states, $\frac{1}{\sqrt{2}}\left(|A\rangle + \mathrm{e}^{i\phi}|B\rangle\right)$, because $D_z = 0 \Leftrightarrow \cos(\theta) = 0 \Leftrightarrow \theta = \pm\frac{\pi}{2}$. This is described in more detail in [13, Hasan and Kane, Rev. Mod. Phys., No. 82 (2010)].

Breaking either symmetry opens a gap in the Dirac cone allowing for massive states to exist. For example, the difference in energy on the atomic sites adds a term proportional to the third Pauli matrix, σ_z, the existence of which allows the state to live on different latitudes of the Bloch sphere than just the equator. When the system undergoes a closed loop in one or more parameters it allows the state to trace out a closed loop on the Bloch sphere, acquiring in the process a phase proportional to the solid angle traced out, see figure 3.

For this all to work it is necessary to be able to excite specifically the electrons in one valley (the now gapped Dirac cone) to be the sole source of the Berry curvature, as exciting both leads to mutual cancellation (applying the time-reversal operator to both sides of equation (2.36) shows that the Berry curvature is odd in momentum, $\mathbf{\Omega}(-k) = -\mathbf{\Omega}(k)$).

2.6.1 The Haldane Model and the Valley Hall Effect

One model that leads to physics as described above is the Haldane model [16]. The following shows how to get a Hamiltonian on the form of equation (2.41). The Haldane model is very similar to the one of hexagonal Boron-Nitride described above. In fact, the Boron-Nitride model is a special case of the Haldane model. It contains the honeycomb lattice with two different sublattices with different on-site energy. Where it differs is in that it includes next-nearest neighbour hopping (inter-sublattice hopping, i.e. hopping to the same species of atom in another primitive unit cell) and a local magnetic flux penetrating the plane of the 2D lattice in such a way that there is no net flux through the Wigner-Seitz unit cell. A way to do this is to have a periodic vector potential with a maximum in the middle of the Wigner-Seitz cell, equidistant to each inhabitant in that unit cell. With this setup the magnetic flux is arranged such that a jump to a next-nearest neighbour incurs a phase phactor, $\mathrm{e}^{\pm i\phi}$, with the sign depending on the direction of the jump, see figure 4, while a jump to nearest neighbour will be phaseless.

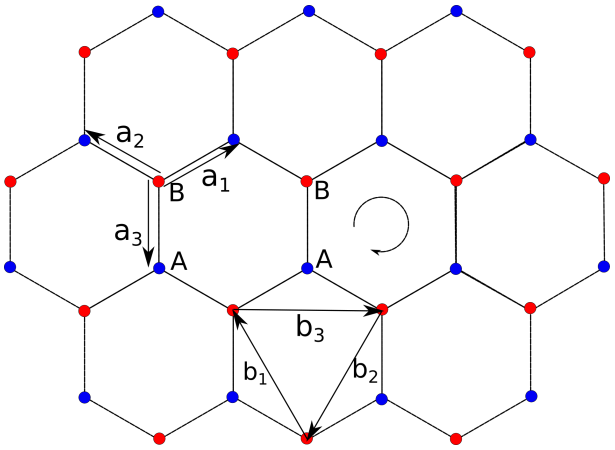

Figure 4: The Haldane lattice, consisting of 2 atom species, A (blue) and B (red), arranged in a honeycomb lattice. The nearest- and next-nearest neighbour hopping vectors, $\mathbf{a}_i$ and $\mathbf{b}_i$ respectively, are indicated and the direction of positive phase gain due to the local magnetic flux is drawn as a (clockwise) circular arrow.

The A and B atoms will be taken to have on-site energies of $\pm M$, and the nearest- and next-nearest neighbour hopping energies will be t_1 and t_2, respectively. The different on-site energies break inversion symmetry while the magnetic field breaks time reversal symmetry. The vectors from a B-atom to its nearest A-atoms are called $\mathbf{a}_i$ (with the distance between neighbouring particles a_0) and the vectors starting from one atom and pointing to another of the same species within the same Wigner-Seitz unit cell are called $\mathbf{b}_i$. Both sets are indicated on figure 4 and they are given by

$$\mathbf{a}_1 = \frac{1}{2}\begin{pmatrix} \sqrt{3} \\ 1 \end{pmatrix} a_0, \quad \mathbf{a}_2 = \frac{1}{2}\begin{pmatrix} -\sqrt{3} \\ 1 \end{pmatrix} a_0, \quad \mathbf{a}_3 = \begin{pmatrix} 0 \\ -1 \end{pmatrix} a_0 \tag{2.43}$$

and

$$\mathbf{b}_1 = \frac{1}{2}\begin{pmatrix} -\sqrt{3} \\ 3 \end{pmatrix} a_0, \quad \mathbf{b}_2 = \frac{1}{2}\begin{pmatrix} -\sqrt{3} \\ -3 \end{pmatrix} a_0, \quad \mathbf{b}_3 = \begin{pmatrix} \sqrt{3} \\ 0 \end{pmatrix} a_0. \tag{2.44}$$

Each atom has 3 nearest neighbours and 6 next-nearest neighbours.
With all these building blocks, we get a Hamiltonian (on a "site-spinor" form) that looks like

$$
\begin{aligned}
H = \sum_{\lambda} \Big\{ & M \left(|A\lambda\rangle \langle A\lambda| - |B\lambda\rangle \langle B\lambda| \right) \\
& + t_1 \Big[|A\lambda\rangle \langle B\lambda| + |A\lambda + \mathbf{b}_2\rangle \langle B\lambda| + |A\lambda - \mathbf{b}_3\rangle \langle B\lambda| \\
& \quad + |B\lambda\rangle \langle A\lambda| + |B\lambda - \mathbf{b}_2\rangle \langle A\lambda| + |B\lambda + \mathbf{b}_3\rangle \langle A\lambda| \Big] \\
& + t_2 \Big[\Big((|A\lambda + \mathbf{b}_1\rangle + |A\lambda + \mathbf{b}_2\rangle + |A\lambda + \mathbf{b}_3\rangle) \mathrm{e}^{-i\phi} \\
& \quad + (|A\lambda - \mathbf{b}_1\rangle + |A\lambda - \mathbf{b}_2\rangle + |A\lambda - \mathbf{b}_3\rangle) \mathrm{e}^{+i\phi} \Big) \langle A\lambda| \\
& \quad + \Big((|B\lambda + \mathbf{b}_1\rangle + |B\lambda + \mathbf{b}_2\rangle + |B\lambda + \mathbf{b}_3\rangle) \mathrm{e}^{i\phi} \\
& \quad + (|B\lambda - \mathbf{b}_1\rangle + |B\lambda - \mathbf{b}_2\rangle + |B\lambda - \mathbf{b}_3\rangle) \mathrm{e}^{-i\phi} \Big) \langle B\lambda| \Big] \Big\},
\end{aligned}
\tag{2.45}
$$

where λ is a vector indicating the unit cell in question. The first line represents the difference in on-site energy. The first square bracket, proportional to t_1, are the hoppings from a site to its 3 nearest neighbours (of different atom species). The last square bracket, with terms proprtional to t_2, account for the next-nearest neighbour hopping, all to atoms of the same species, but within different primitive unit cells. This fearsome expression can be tamed a bit when we Fourier transform it using $|X\lambda\rangle = \sum_{\mathbf{k}} |X\mathbf{k}\rangle \, \mathrm{e}^{i\mathbf{k}\cdot\lambda}$; every single term will have its only dependence on λ of the form $\mathrm{e}^{\pm i(\mathbf{k}-\mathbf{k}')\cdot\lambda}$, and completing the λ and $\mathbf{k}'$ sums (the first of which yields a delta function in $\mathbf{k}$ and $\mathbf{k}'$) leaves us with

$$
\begin{aligned}
H = \sum_{\mathbf{k}} \Big\{ & M \left(|A\mathbf{k}\rangle \langle A\mathbf{k}| - |B\mathbf{k}\rangle \langle B\mathbf{k}| \right) \\
& + t_1 |A\mathbf{k}\rangle \langle B\mathbf{k}| \left(1 + \mathrm{e}^{i\mathbf{b}_2\cdot\mathbf{k}} + \mathrm{e}^{-i\mathbf{b}_3\cdot\mathbf{k}} \right) + t_1 |B\mathbf{k}\rangle \langle A\mathbf{k}| \left(1 + \mathrm{e}^{-i\mathbf{b}_2\cdot\mathbf{k}} + \mathrm{e}^{\mathbf{b}_3\cdot\mathbf{k}} \right) \\
& t_2 \Big[|A\mathbf{k}\rangle \langle A\mathbf{k}| \sum_j \left(\mathrm{e}^{-i\phi + i\mathbf{b}_j\cdot\mathbf{k}} + \mathrm{e}^{i\phi - i\mathbf{b}_j\cdot\mathbf{k}} \right) + |B\mathbf{k}\rangle \langle B\mathbf{k}| \sum_j \left(\mathrm{e}^{i\phi + i\mathbf{b}_j\cdot\mathbf{k}} + \mathrm{e}^{-i\phi - i\mathbf{b}_j\cdot\mathbf{k}} \right) \Big] \Big\}
\end{aligned}
\tag{2.46}
$$

The terms in parentheses proportional to t_1 can be written as $\exp(\mp i\mathbf{a}_1\cdot\mathbf{k}) \sum_j \exp(\pm i\mathbf{a}_j\cdot\mathbf{k})$ by using the fact that the next-nearest jump vectors can be created from a combination of nearest neighbour jump vectors. The first phase factor can be gauged away by applying a unitary transformation (rotation) that commutes with the rest of the Hamiltonian, $u = \exp(i\mathbf{a}_1\cdot\mathbf{k}\sigma_z/2)$, where σ_z is the third Pauli matrix (see equation (2.42)) in our site-spinor space. Applying this "operator" from the right and its hermitian conjugate from the left, writing out the exponentials as cosines and sines and using the trigonometric identity for sums of angles we get

$$
\begin{aligned}
H(\mathbf{k}) = 2t_2 \cos(\phi) \sum_j \cos(\mathbf{b}_j\cdot\mathbf{k}) \mathbb{1} + t_1 \sum_j \left(\cos(\mathbf{a}_j\cdot\mathbf{k})\sigma_x + \sin(\mathbf{a}_j\cdot\mathbf{k})\sigma_y \right) \\
+ \left(M - 2t_2 \sin(\phi) \sum_j \sin(\mathbf{b}_j\cdot\mathbf{k}) \right) \sigma_z.
\end{aligned}
\tag{2.47}
$$

When written on this form the dispersion follows readily,

$$\epsilon(\mathbf{k}) = 2t_2\cos(\phi)\sum_j \cos(\mathbf{b}_j\cdot\mathbf{k}) \pm\sqrt{t_1^2\sum_{ij}\left[\cos(\mathbf{b}_i\cdot\mathbf{k})\cos(\mathbf{b}_j\cdot\mathbf{k})+\sin(\mathbf{b}_i\cdot\mathbf{k})\sin(\mathbf{b}_j\cdot\mathbf{k})\right]+\left(M-2t_2\sin(\phi)\sum_j\sin(\mathbf{b}_j\cdot\mathbf{k})\right)^2}. \tag{2.48}$$

This shows a two-band structure with a gap that closes when the term under the square root disappears. There are two such points where this is possible, the Dirac points, corresponding to the two points in the Brillouin zone where $\mathbf{b}_j\cdot\mathbf{k} = \pm\frac{2\pi}{3}$, and it only happens if $M = \pm 3\sqrt{3}t_2\sin(\phi)$. The Dirac points are placed at $\mathbf{k} = \mathbf{K}_\pm$, where

$$\mathbf{K}_\pm = \pm\begin{pmatrix}\frac{4\pi}{3\sqrt{3}a_0}\\ 0\end{pmatrix}. \tag{2.49}$$

If there is no magnetic flux then the phase gained when making a next-nearest neighbour jump is 0, which means that the gap closes for $M = 0$ (note that this specifically kills the coefficients of σ_z and has the consequences discussed in chapter 2.6). The Dirac points are placed in opposite corners of the Brillouin zone which itself takes the form of a rotated (by $\pi/2$) honeycomb structure. Let the choice of Dirac point be indicated by $\alpha = \pm 1$ in the following. A linearization around a Dirac point $\mathbf{K}_\alpha$ with a new, small deviation from the cone of choice, $\mathbf{k} = \mathbf{k}' - \mathbf{K}_\alpha$, where $\mathbf{k}'$ is the full k-vector, gives us (after discarding the term proportional to $\mathbb{1}$)

$$H_\alpha = -v\left(p_x\sigma_x + \alpha p_y\sigma_y\right) + D\sigma_z, \tag{2.50}$$

where $v = \frac{3a_0t_1}{2\hbar}$, $p_i = \hbar k_i$ and $D = M - 3\sqrt{3}\alpha t_2\sin(\phi)$. Here we could make a spatial inversion to make the sign in front of the term in parentheses to become positive, but, since it has no physical consequences, we will keep it.
Equation (2.50) has the split energies

$$\epsilon(\mathbf{k})_\pm = \pm\sqrt{v^2p^2 + D^2} \tag{2.51}$$

and the eigenstates

$$|\pm\rangle = \frac{1}{\sqrt{v^2p^2 + (D-\epsilon_\pm)^2}}\begin{pmatrix}v(p_x - ip_y)\\ D-\epsilon_\pm\end{pmatrix}. \tag{2.52}$$

The energies are plotted with and without the gap opening in figure 5.

Rote insertion into equation (2.18) gives an expression for the k_x-k_y-component of the Berry curvature (equivalent to the z-component of the Berry curvature, see equation (2.14)) for the valence band,

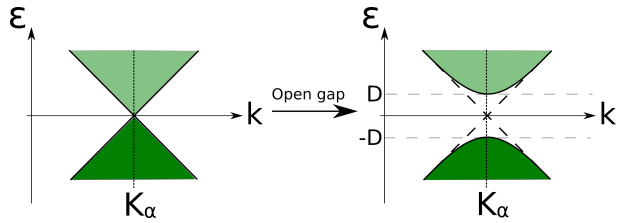

Figure 5: A 2D cross-section of a Dirac cone centered at $\mathbf{K}_\alpha$, before and after a gap opens due to either of the two mentioned mechanisms.

$$\Omega_{k_x k_y} = -\frac{\alpha}{2}\frac{v^2\hbar^2 D}{\left(v^2p^2 + D^2\right)^{3/2}}, \tag{2.53}$$

where, as before, $\alpha = \pm 1$ indicates the choice of Dirac cone. We see here that when neither inversion symmetry nor time reversal symmetry are broken ($D = 0$) then the Berry curvature vanishes everywhere except for $|k| = 0$, where the gap closes. At this point the Berry curvature diverges. Opening the gap allows for a finite Berry curvature throughout k-space.

To get the conductivity we should use equation (2.40) together with the Berry curvature from the exact expression for the Hamiltonian, equation (2.47), and its eigenstates, but integrating across a hexagonal Brillouin zone is tedious work. Instead, we can calculate the contribution to the conductivity in the vicinity of the Dirac cone and make use of the fact that the Chern number is conserved under smooth deformation to significantly simplify this integration; by making the gap small ($D << v\hbar/a_0$) we can make equation (2.53) similar to a delta function, making the integration easy. In other words, when the gap is small then the area around the gap is the main contributor to the Berry curvature.
By making the substitutions $\frac{g}{a_0} = \frac{D}{v\hbar}$ and $|y| = |k|a_0$ we get

$$\sigma_{xy} = -\frac{\alpha}{2}\frac{e^2}{h}\int \frac{d^2y}{2\pi}\frac{g}{\left(y^2+g^2\right)^{3/2}} \overset{g\to 0}{\approx} -\mathrm{sgn}(D)\frac{\alpha}{2}\frac{e^2}{h}, \tag{2.54}$$

where the limits of integration are large enough to capture the bulk of the contributions and the sign of D determines whether the Berry curvature resembles a positive or negative delta function.
We see here that the sign of $D = M - 3\sqrt{3}\alpha t_2 \sin(\phi)$ is important when considering both Dirac cones. We will, for simplicity, just outline the two simplest cases:
If $t_2 \sin(\phi) = 0$, i.e. there is no change in phase when hopping to a next-nearest neighbour or no hopping at all, then the contributions from the two cones cancel. It is still possible to get a non-zero transverse conductivity by only exciting the particles in one cone across the gap to the respective conduction cone, with methods specific to the material at hand.
On the contrary, if $M = 0$ and $t_2 \sin(\phi) \neq 0$, i.e. there is no difference in on-site energy, but next nearest neighbour hopping is allowed and the phase gained from such a hop is different from an integer number of π, then we get the same sign for the two cones and the resulting Chern number for the two cones add up to 1, resulting in a transverse conductivity $\sigma_{xy} = \pm\frac{e^2}{h}$.

3 Magnetoplasmons in 3-Dimensional Charge-Fluid

This chapter follows the progression of the works of Alexander Fetter, [4], with additional steps shown to better illustrate the methods used to obtain the results found.
Before we enter the realm of Berry plasmons it would be wise to first examine the simpler (and better understood) case of zero-field plasmons and (chiral) magnetoplasmons. Plasmons are collective excitations of charge carriers that manifest themselves as charge density waves in the material in which they live. These plasmons generally come in two flavors; the bulk modes and the edge modes. The bulk modes have the charge carriers in the bulk of the material moving according to the given mode, while the edge modes, as we will see, are confined to the edge, their amplitudes decaying exponentially further toward the bulk.

The simplest case to consider where both bulk and edge modes are present is that of a semi-infinite three-dimensional half-space, infinite in the y- and z-directions and inhabiting the $x < 0$ half. We will first consider a small toy model just to introduce the idea of plasmons, then follow up with the fully infinite three-dimensional bulk system and finally add the edge to make it a half-space when we want to examine the edge modes. Other geometries will be considered further on in this analysis.

3.1 A Toy Model for Bulk Plasmons

The "infinite" wave-length bulk plasmon is both easy to visualize as a thought experiment and leads to the famous plasmon bulk frequency which we will see in many iterations throughout this thesis, so we will let this be the starting point of our introduction to plasmons. This will be done by imagining a box with side lengths (L_x, L_y, L_z) of "jellium", an electron fluid resting on a static positive background with density n_0. The entire negative charge density is displaced a distance χ in the x-direction compared to the positive background (for example with an external electric field), as pictured in figure 6, where χ is small compared to the length of the box, $\chi << L_x$. If the distance between the two regions of positive and negative charge is small compared to the height and width of the box, $L_x << L_y, L_z$, then the electric field between the two regions is similar to that of a plate capacitor, $E = V/L_x$. The voltage difference is dependent on the total charge stored on the plates, Q, and the geometry, $V = \frac{4\pi Q L_x}{\epsilon L_y L_z}$. The total charge is the charge density integrated over the geometry of the box, made easy by the constant density, so that $Q = -en_0\chi L_y L_z$, which leads to an electric field $E = \frac{-4\pi e n_0 \chi}{\epsilon}$. The equation of motion for the displacement is then finally $\ddot{\chi} = \frac{eE}{m} = -\frac{4\pi e^2 n_0}{m\epsilon}\chi$, which has harmonic solutions with frequency $\Omega_p = \sqrt{\frac{4\pi n_0 e^2}{m\epsilon}}$. This result is independent of the system size, so scaling the system to an infinite size then yields the infinite wave-length bulk plasmon.

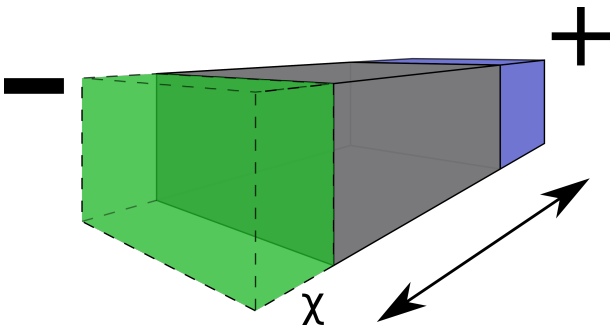

Figure 6: Visualization of the toy model or a cutout of the bulk plasmon in 3 dimensions. It is a collective mode of the electron fluid, and in the long wavelength limit and in the absence of magnetic field it moves in unison at frequency $\omega = \Omega_p$. A magnetic field would cause the movement to be elliptical rather than unidirectional.

3.2 Bulk Plasmons in 3D

We will quickly outline the method of getting the dispersion of a zero-field, finite wave-length bulk plasmon in 3D before we gradually add elements that complicate the calculation. We model our system as material consisting of a rigid positive background density, en_0, with $-e < 0$ the electron charge, and an electron fluid of local charge density $-e(n_0 + n)$, where n is the density perturbation. Two main equations govern the motion of our fluid; The continuity equation,

$$\frac{\partial}{\partial t} n + n_0 \nabla \cdot \mathbf{v} = 0, \tag{3.1}$$

keeps track of charge conservation by relating the change of the local (charge) density at a point with the associated velocity, $\mathbf{v}$, while the Euler equation,

$$\frac{\partial}{\partial t} \mathbf{v} = -\frac{s^2}{n_0} \nabla n + \frac{e}{m} \nabla \Phi, \tag{3.2}$$

keeps track of the force on charge elements from the electrostatic potential, Φ, caused by the displacement of charges from their unperturbed state. $\mathbf{v}$ is the velocity field of the charge elements and m is the effective collective excitation mass of the plasmon. Here we have added a dispersion term caused by mechanical pressure where $s^2 = \frac{1}{m} \frac{\partial p}{\partial n}$ is the squared effective wave speed when no magnetic field is active. In the long wavelength limit this will, as we will see, be negligible compared to the other contributions to the dispersion.
The Poisson equation provides a relation between the potential and the charge density,

$$\nabla^2 \Phi = 4\pi e n, \tag{3.3}$$

where we, for simplicity, have assumed that the dielectric constant of the background is the identity, $\epsilon = 1$. The system has translational invariance and we are looking for solutions after the system has reached a steady state so that the solution will be of a plane-wave form, $n \propto \mathrm{e}^{i(\mathbf{q}\cdot\mathbf{r} - \omega t)}$. We can take the divergence on both sides of equation (3.2), insert equation (3.1) and (3.3) and use that $\nabla^2 n = -q^2 n$ to get

$$\omega^2 \frac{n}{n_0} = \frac{e}{m} 4\pi e n + \frac{s^2}{n_0} q^2 n. \tag{3.4}$$

Here we can cancel factors of n and multiply by n_0 on both sides and introduce the bulk 3-dimensional plasma frequency (with dielectric constant $\epsilon = 1$) $\Omega_p = \left(\frac{4\pi e^2 n_0}{m}\right)^{1/2}$ to rewrite this as a final expression

$$\omega^2 = \Omega_p^2 + s^2 q^2. \tag{3.5}$$

In the long wavelength case where $\Omega_p^2 >> s^2 q^2$, this simply reduces to $\omega = \pm\Omega_p$. Figure 6 can be seen as a cutout of a small section of a bulk plasmon, featuring one wave top and one wave valley in the density.

3.3 Bulk Magnetoplasmons in 3D

From here we want to complicate things a bit. A magnetic field is placed along the z-direction, $\mathbf{B} = B\hat{z}$. The particles are acted on by the magnetic field through the cyclotron frequency, $\omega_c = \frac{eB}{mc}$ (the inclusion of c is only in Gaussian units, which we will be using for now, and not in SI units). The electromagnetic force will be treated completely non-relativistically (instant propagation, no retardation) so that the Euler equation takes on the form

$$\frac{\partial}{\partial t}\mathbf{v} + \frac{\mathbf{v}}{\tau} = -\frac{s^2}{n_0}\nabla n + \frac{e}{m}\nabla\Phi + \omega_c \hat{z} \times \mathbf{v}. \tag{3.6}$$

In equation (3.6) we have included a decay term with mean collison time, τ, that allows for a finite lifetime of the mode due to scattering on impurities. Both the decay term and the mechnical pressure terms will, in general, be neglected further on for simplicity. The relationship between electrostatic potential and charge density is still governed by equation (3.3). The effect of the magnetic field will primarily be felt in the x-y-plane and so we will let $\mathbf{q}$ live in this plane. Taking the divergence $(\nabla\cdot)$ on both sides of equation (3.6), inserting equations (3.1) and (3.3) and using the fact that $\nabla \cdot (\hat{z} \times \mathbf{v}) = -\hat{z} \cdot \nabla \times \mathbf{v}$ we get

$$(\omega^2 + \frac{i\omega}{\tau})\frac{n}{n_0} = s^2 q^2 \frac{n}{n_0} + \frac{4\pi e^2}{m} n - \omega_c \hat{z} \cdot \nabla \times \mathbf{v}. \tag{3.7}$$

To find an expression for the curl of the velocity, apply $\nabla\times$ from the left to equation (3.6) and use that $\nabla \times \hat{z} \times \mathbf{v} = \hat{z}(\nabla \cdot \mathbf{v}) - (\hat{z} \cdot \nabla)\mathbf{v}$ together with equation (3.1) to get

$$\begin{aligned} &\nabla \times \mathbf{v} \frac{1}{i}\left(\omega + \frac{i}{\tau}\right) = \omega_c \nabla \times (\hat{z} \times \mathbf{v}) \\ &\Leftrightarrow \nabla \times \mathbf{v} = -\omega\omega_c \left(\omega + \frac{i}{\tau}\right)^{-1} \frac{n}{n_0}\hat{z}. \end{aligned} \tag{3.8}$$

Combining equations (3.7) and (3.8) and multiplying through by $\frac{n_0}{n}$ we get

$$\omega\left(\omega+\frac{i}{\tau}\right)=s^2q^2+\frac{4\pi e^2n_0}{m}+\omega_c^2\omega\left(\omega+\frac{i}{\tau}\right)^{-1}. \tag{3.9}$$

Introducing the effective colission-corrected frequency $\tilde{\omega}=\left(\omega+\frac{i}{\tau}\right)$ we can rearrange to get a final dispersion relation,

$$\frac{\omega}{\tilde{\omega}}\left(\tilde{\omega}^2-\omega_c^2\right)=s^2q^2+\Omega_p^2. \tag{3.10}$$

If the average collision time is large, such that $\omega >> \frac{1}{\tau}$, then equation (3.10) simplifies nicely to

$$\omega^2=s^2q^2+\Omega_p^2+\omega_c^2, \tag{3.11}$$

where we see that the squared frequency grows linearly with the squared magnitude of the magnetic field and the squared crystal momentum.

3.4 Surface Plasmons in 3D

When we introduce the edge at $x=0$ we break translational invariance along the x-direction. Let $x<0$ be the space occupied by the material and $x>0$ be vaccuum. We will still have plane waves propagating along the y-z-plane, but the effects of the magnetic field, $\mathbf{B}=B\hat{z}$, will only be felt in the y-direction due to the transverse nature of the Lorentz force. For that reason we will limit q to lie along the y-direction.

Equations (3.1) and (3.6) still hold, but we will now have two Poisson equations, one for each region;

$$\nabla^2\Phi_<=4\pi en, \tag{3.12}$$

and

$$\nabla^2\Phi_>=0, \tag{3.13}$$

where the subscript $<$ indicates that we are in the $x<0$ region where our material lives and the subscript $>$ indicates that we are in the empty region of $x>0$. With q along the y-direction the Laplacian now has the form $\nabla^2=(\frac{\partial^2}{\partial x^2}-q^2)$.

To ensure that there is no potential to be felt infinitely far away from the material, we will need to enforce the condition that $\Phi\to 0$ as $x\to\infty$, and we will also need it to be bounded deep in the material which means that as $x\to-\infty$ the potential should trend toward a finite value. We also need to ensure that the potential and the x-component of the electric field are continuous across the boundary.

Equation (3.13) then has a solution of the form

$$\Phi_>(x)=\Phi_0\mathrm{e}^{-qx}. \tag{3.14}$$

Equation (3.12) is non-trivial to solve because of the appearance of the function $n(x)$ on the right hand side. We will assume that the solutions are of an exponential form. This means that inside the material we have two solutions, one for the homogenous equation and one particular solution. The particular solution is $e^{\kappa x}$, for some κ, which can be either real or imaginary, that we will solve for. If κ is real the modes that survive our boundary conditions will decay exponentially away from the surface, and we have our localised surface modes. If κ is imaginary then the situation is very reminiscent of that of a bulk plasmon; it acts as plane waves bouncing off the surface, with a dispersion similar to that of bulk plasmons with $q^2 \to q^2 - \kappa^2$, as we will see in equation (3.15) in a bit. The homogeneous solution is e^{qx}, reminiscent of what we see from the other side of the boundary, but with the sign of the exponent flipped because we are in the region of negative x. It shows how the potential resulting from the charge density wave is very evident close to the surface where the mode lives, but it gets washed out as you move into the bulk and the potential from the alternately charged regions at the edge starts averaging out to zero.

Inserting the particular solution in equation (3.12) gives a relation between κ and q and applying the Laplacian operator again shows that we now have $\nabla^2 n = (\kappa^2 - q^2)n$. The method is the exact same as in section 3.2 above except for the new term, κ, arising from the fact that the x-direction is treated differently from the y-direction. Repeating the steps of eliminating the potential and density in equation (3.6) above leaves us with

$$\kappa^2 = q^2 + \frac{1}{s^2}\left(\Omega_p^2 - \frac{\omega}{\tilde{\omega}}(\tilde{\omega}^2 - \omega_c^2)\right) \tag{3.15}$$

We are interested in the surface modes and will therefore treat κ as real and positive (to keep the pontential bounded) and so the potential has an x-dependence of the form

$$\Phi_<(x) = \Phi_1 e^{qx} + \Phi_2 e^{\kappa x}. \tag{3.16}$$

Equations (3.15) and (3.16) show that the confinement of the potential scales with q, with large q, corresponding to short wavelength, leading to a highly confined potential. To determine the coefficients we need to get an expression on which we can impose our boundary condition. Let us first combine equations (3.12), (3.15) and (3.16) to express the density in terms of the potential,

$$n = \frac{\Omega_p^2 + \frac{\omega}{\tilde{\omega}}\left(\omega_c^2 - \tilde{\omega}^2\right)}{4\pi e s^2}\Phi_2 e^{\kappa x}. \tag{3.17}$$

From here we can look at the x- and y-components of equation (3.6). The magnetic field mixes the terms, so isolating v_y and inserting it in the expression for v_x, multiplying by $4\pi e n_0$ and recognising terms that include $\frac{4\pi e^2 n_0}{m} = \Omega_p^2$ and rearranging leaves us with

$$4\pi e n_0 v_x = \frac{iq\Omega_p^2}{\tilde{\omega} - \omega_c}\Phi_1 e^{qx} + i\left(\kappa\tilde{\omega} + q\omega_c\right)\frac{\omega}{\tilde{\omega}}\Phi_2 e^{\kappa x}. \tag{3.18}$$

Imposing our boundary conditions of continuous potential across the boundary leads to

$$\Phi_0 = \Phi_1 + \Phi_2, \tag{3.19}$$

and the condition of continuous electric field (or, equivalently, -$\frac{\partial\Phi}{\partial x}$) leads to

$$q\Phi_1 + \kappa\Phi_2 = -q\Phi_0 = -q\left(\Phi_1 + \Phi_2\right). \tag{3.20}$$

These two conditions along with imposing the regular fluid dynamical boundary condition that there should be no flow through the edge, that $v_x(x=0)=0$, on equation (3.18) leads to the expression

$$0 = \left(-i\frac{\Omega_p^2(\kappa+q)}{2(\tilde{\omega}-\omega_c)} + i(\kappa\omega + q\omega_c)\frac{\omega}{\tilde{\omega}}\right)\Phi_2, \tag{3.21}$$

which, if the term on the right is to be equal to that on the left, leads to the dispersion relation for the surface modes,

$$2\left(\kappa\tilde{\omega} + q\omega_c\right) = \frac{\tilde{\omega}}{\omega}\frac{(\kappa+q)\Omega_p^2}{\tilde{\omega}-\omega_c}. \tag{3.22}$$

This is significantly simplified when considering the case of no damping (collisionless limit) where $\tilde{\omega}=\omega$, and even moreso when considering the long wave-length limit[1], where $q << \Omega_p/s$, in which case equation (3.22) reduces to

$$\omega^2 - \omega_c\omega - \frac{\Omega_p^2}{2} = 0. \tag{3.23}$$

The solutions can be written as a positive mode (assuming positive ω_c, otherwise just reverse directions) travelling along the y-direction toward increasing y, and a negative mode, travelling toward decreasing y,

$$\omega_+ = \frac{1}{2}\mathrm{sgn}(\omega_c)\left[\sqrt{2\Omega_p^2+\omega_c^2} + |\omega_c|\right] \tag{3.24a}$$

$$\omega_- = -\frac{1}{2}\mathrm{sgn}(\omega_c)\left[\sqrt{2\Omega_p^2+\omega_c^2} - |\omega_c|\right]. \tag{3.24b}$$

When the magnetic field is turned off we get degenerate modes with frequency $\omega = \pm\frac{\Omega_p}{\sqrt{2}}$ as initially predicted by Ritchie [7].

Note that the frequency of the "plus-mode" grows with increasing magnetic field strength while the "minus-mode" shrinks with increasing field strength, see figure 7. Given knowledge of the parameters of the system the modes are distinguishable solely by their direction or magnitude. This is our first glimpse of the chiral nature of the surface modes and it will be a reoccurring phenomenon throughout this examination of the edge plasmon phenomenon.

4 Magnetoplasmons on a Semi-Infinite (Half-)Plane

In this chapter we will, similarly to chapter 3, follow the works of Fetter, references [4] and [5], with additional steps shown, as this gives a good introduction to the new challenges that arise from being limited to two dimensions.

[1] These assumptions will be made repeatedly throughout this paper.

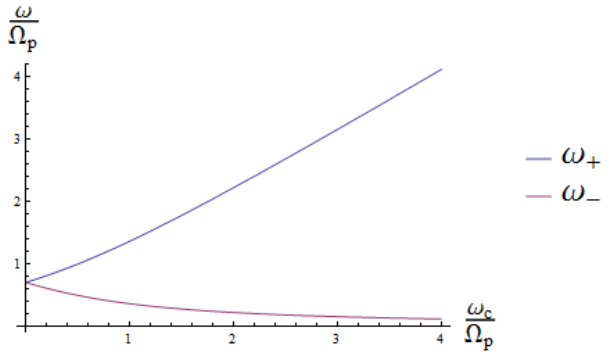

Figure 7: The un-signed frequencies of the 3D surface plasmon mode as a function of magnetic field, given in units of the bulk plasmon frequency, Ω_p.

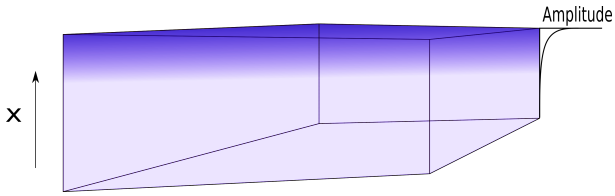

Figure 8: Infinite half-space occupying the negative x-region. The dark blue indicates the edge mode and the opaqueness/density indicates the amplitude. The plasmon mode is exponentially confined to the edge.

Bulk magnetoplasmons in two dimensions can be treated very similarly to the bulk plasmons in three dimensions, with the small change that the Poisson equation needs a delta function in one direction (preferably the same direction as the magnetic field; only the part of the magnetic field that is perpendicular to the plane will affect the behaviour of the plasmon mode), $\nabla^2\Phi = 4\pi en\delta(z)$, for a plane in the x-y-plane with background dielectric constant $\epsilon = 1$. Integration across a small gap in the z-direction together with the requirement that the potential vanish infinitely far away from the plane allows us to solve for an in-plane expression for the potential. On either side of the disk, we just have the familiar Poisson equation, $\left(\frac{\partial^2}{\partial z^2} - q^2\right)\Phi = 0$ with the familiar solutions, $\Phi = \Phi_0 e^{\pm qz}$, with q the in-plane wave-vector. The integration across $z = 0$ gives us a jump condition for the potential,

$$\frac{\partial}{\partial z}\Phi|_{0^+} - \frac{\partial}{\partial z}\Phi|_{0^-} = 4\pi en, \tag{4.1}$$

which can be used to find the constant Φ_0. Using the derivatives above and below gives us the z-depence of the potential, $\Phi(z) = -\frac{2\pi en}{q}e^{-q|z|}$, which has in-plane component $\Phi(z=0) = -\frac{2\pi en}{q}$. Taking the in-plane Laplacian then gives us a more easily insertable Poisson equation,

$$\nabla_2^2\Phi(z=0) = -q^2\Phi(z=0) = 2\pi nq, \tag{4.2}$$

where ∇_2^2 is the in-plane Laplacian. Applying the steps detailed in chapter 3.2 then yields a dispersion relation that is strikingly similar, namely

$$\omega^2 = \Omega_q^2 + \omega_c^2 + s^2 q^2, \tag{4.3}$$

where q is the in-plane wavevector and

$$\Omega_q^2 = \frac{2\pi e^2 n_0}{m} q, \tag{4.4}$$

is the new q-dependent bulk plasmon frequency.

The case of the edge magnetoplasmons in the geometry of a two-dimensional half-plane (infinite in the y-direction but finite in x) is covered in the same article by Fetter as described above, [4], as well as in [5]. In the two papers he employs different methods with different boundary conditions, and we will here briefly introduce the considerations made, the methods used, and the results obtained.

In [4] Fetter approaches the problem of the two-dimensional half-plane very similarly to the approach he used to get the dispersion of plasmons in the three-dimensional half-space. The magnetic field is still pointed in the z-direction (orthogonal to the plane) and the same boundary condition of having no velocity in the x-direction (perpendicular to the edge) near the edge is used to lead to the final dispersion relation. Where the two cases differ is when considering the Poisson equation, since we now have yet another limit to our charge density: it lives only on the negative-x half. This is represented with a Heaviside step function,

$$\nabla^2 \Phi = \left(\frac{\partial^2}{\partial x^2} - q^2 + \frac{\partial^2}{\partial z^2} \right) \Phi = 4\pi e n(x) \delta(z) \Theta(-x). \tag{4.5}$$

Fourier transforming the x-component of this expression gives

$$\left(-k^2 - q^2 + \frac{\partial^2}{\partial z^2} \right) \bar{\Phi}(k, z) = 4\pi e \delta(z) \int_{-\infty}^{0} dx \mathrm{e}^{-ikx} n(x) \equiv 4\pi e \delta(z) \bar{n}(k), \tag{4.6}$$

which can be treated in a manner identical that of the bulk, with a jump condition akin to equation (4.1), followed by an inverse Fourier transformation. This, however, leads a problem for further analytical analysis.

When considering the connection between the in-plane electrostatic potential and the charge density in two dimensions, one gets a non-local relation with a kernel, $\Phi(x) = -4\pi e \int_{-\infty}^{0} dx' K(x - x') n(x')$. This kernel is the usual 2D Coulomb interaction kernel,

$$K(x) = \frac{1}{2} \int_{-\infty}^{\infty} \frac{dk}{2\pi} \frac{\mathrm{e}^{ikx}}{\sqrt{k^2 + q^2}} = \frac{1}{2\pi} K_0(q|x|), \tag{4.7}$$

where k is the wavevector in the direction that has been cut off, which, in this case, is x, and K_0 is the 0^{th} modified Bessel function of the second kind. To deal with the nonlocality of the kernel (the fact that the potential needs "information" about the density at all points instead of just at the point at which we are evaluating the potential) an approximate kernel resulting in a Coulomb interaction with longer range than usual is introduced,

$$K'(x) = \int_{-\infty}^{\infty} \frac{dk}{2\pi} \frac{q \mathrm{e}^{ikx}}{k^2 + 2q^2} = 2^{-3/2} \mathrm{e}^{-\sqrt{2}q|x|}. \tag{4.8}$$

This has the benefit of significantly simplifying the potential-density relation, since the new kernel is the Green's function of a simple operator, $\left[\partial_x^2 - 2q^2\right] K'(x-x') = -q\delta(x-x')$, such that

$$(\partial_x^2 - 2q^2)\Phi_< = 4\pi eqn(x) \tag{4.9}$$

inside the material ($x < 0$) and

$$(\partial_x^2 - 2q^2)\Phi_> = 0 \tag{4.10}$$

outside the material ($x > 0$). This has the same form as equations (3.12) and (3.13) and the solution method is the same. Following those same steps results in a dispersion relation of the form

$$\omega_+ = \frac{\sqrt{2}}{3}\mathrm{sgn}(\omega_c)\left[\sqrt{3\Omega_q^2 + \omega_c^2} + |\omega_c|\right] \tag{4.11a}$$

$$\omega_- = -\frac{\sqrt{2}}{3}\mathrm{sgn}(\omega_c)\left[\sqrt{3\Omega_q^2 + \omega_c^2} - |\omega_c|\right], \tag{4.11b}$$

very reminiscent of that found in equations (3.24a)-(3.24b), but with the bulk frequency of equation (4.4), where we also see one mode growing with increasing magnetic field and the other decreasing with increasing magnetic field. For large fields we can expand the square root to see that the minus mode becomes inversely proportional to the magnetic field (which we will assume is positive),

$$\omega_- \overset{\text{Large field}}{\approx} -\frac{1}{\sqrt{2}}\frac{\Omega_q^2}{\omega_c}. \tag{4.12}$$

When the magnetic field is turned off we get the degenerate relation

$$\omega \overset{\text{B=0}}{=} \pm\sqrt{\frac{2}{3}}\Omega_q. \tag{4.13}$$

In [5] Fetter employs a similar, albeit slightly different, approach to the case of the half-plane. Here he formulates the problem in terms of currents and conductivities where he imposes a step-function behaviour on the conductivity in the x-direction rather than forcing the current into the boundary to be 0. This causes the electron density to get an edge term, localised on the edge via a delta function. The consequence of this is that a non-zero current flowing into the edge builds up instead of escaping the system, such that the continuity equation is still valid, essentially letting $n(x) \to n(x) + n^*\delta(x)$. This pile-up of charge on the edge will cause a discontinuity in the derivative of the potential, $\frac{\partial\Phi(x)}{\partial x}\,|_{x=0}$, see figure 9. This boundary condition will be used we we approach the problem of plasmons in the disk geometry, as the alternative seems unphysical; we consider Hall systems, whether regular or anomalous, and so any electric field normal to the edge must surely push charge into or out of the edge.

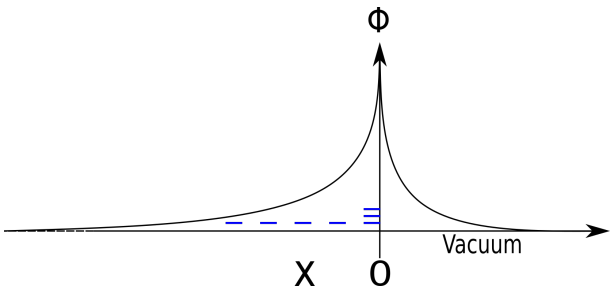

Figure 9: An illustration of the potential at the edge of the material arising due to the build-up of charge and the exponential decay outside the material.

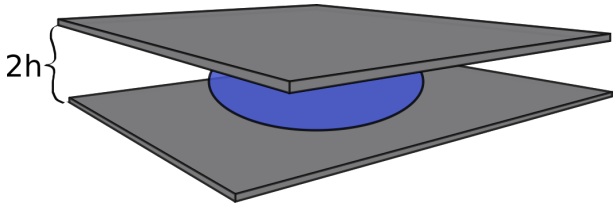

Figure 10: A schematic illustration of the disk-plate setup.

5 The Disk System

In real life infinite systems are expensive, hard to keep clean and adequate storage is hard to come by. Another system that rectifies this, and is suitable for practical use, is that of a two-dimensional disk. It provides a symmetry not dissimmilar to the one-dimensional translation symmetry (up to a phase) along the edge of the infinite half-plane, namely rotational symmetry. In addition, it brings the advantage of being useful in circulator systems since (as the name suggests it should) the edge loops around and meets itself. This means that in a multi-port system, such as those discussed in chapter 1, a signal emerging from one port will traverse the edge and, along the way, possibly meet all the other ports, contrary to the edge of a half-plane where a signal will only potentially meet the ports in the direction of the wave-propagation.

Throughout the remainder of this paper we will consider variants of the following system: We imagine a disk of radius R lying in the x-y-plane, with relative background dielectric constant ϵ, with the possibility of having a magnetic field or Berry curvature pointing in the z-direction. Grounded planes are placed symmetrically a distance h above and below the disk to allow for a change in the behaviour of the Coulomb interaction. This setup is pictured in figure 10.
We assume complete rotational symmetry so, when combined with our desire to find steady-state solutions, we let all angular and temporal dependences be of the form $\mathrm{e}^{i(l\theta-\omega t)}$.

5.1 The Relation Between Electrostatic Potential and Charge Density

This chapter builds on the works of [6], expanding the calculations by showing more in-between steps to make for a clearer derivation.
The disk stretches through the x-y-plane at $z = 0$. Above and below the disk there is no charge and so the potential fulfills equation (3.13), with ∇^2 the cylindrical Laplacian, so the Poisson

equation can be written as

$$\nabla^2\Phi = \frac{4\pi e}{\epsilon} n(r)\Theta(R-r)\delta(z), \tag{5.1}$$

with $\Theta(r)$ the Heaviside step function. The charge being at $z = 0$ means that we can make a "jump-condition" for the derivative of the potential across the disk in the z-direction by integrating a vanishingly small part across $z = 0$, $\lim_{\mu\to 0}\int_{-\mu}^{\mu} dz$.

This gives the folowing relation that needs to be fulfilled (in CGS-units),

$$\frac{\partial\Phi}{\partial z}\,|_{z=0^+} - \frac{\partial\Phi}{\partial z}\,|_{z=0^-} = \frac{4\pi e}{\epsilon} n\Theta(R-r), \tag{5.2}$$

where we have used that $\nabla_2^2\Phi = 0$ for $z \neq 0$, where ∇_2^2 is the in-plane Laplacian.
The next step is to try to find the z-dependence of the potential to ultimately get an in-plane expression for the potential. Outside the disk there is no charge, so the Poisson equation can be written as

$$\begin{aligned}\nabla^2\Phi(r,\theta,z) &= \left[\frac{1}{r}\frac{\partial}{\partial r}r\frac{\partial}{\partial r} + \frac{1}{r^2}\frac{\partial^2}{\partial\theta^2} + \frac{\partial^2}{\partial z^2}\right]\Phi(r,z)\mathrm{e}^{il\theta} \\ &= \left[\frac{1}{r}\frac{\partial}{\partial r}r\frac{\partial}{\partial r} - \frac{l^2}{r^2} + \frac{\partial^2}{\partial z^2}\right]\Phi(r,z)\mathrm{e}^{il\theta} = 0.\end{aligned} \tag{5.3}$$

We can expand $\Phi(r)$ as an infinite sum of Bessel function by doing a Hankel transformation.

$$\bar{\Phi}(p,z) = \int_0^\infty dr r J_l(pr)\Phi(r,z), \tag{5.4}$$

where l is the angular momentum of the relevant mode. This has the inverse transformation

$$\Phi(r,z) = \int_0^\infty dp p J_l(pr)\bar{\Phi}(p,z). \tag{5.5}$$

Inserting this in equation (5.3) and using $u = pr$ we get

$$\int_0^\infty dpp\left[\left(u\frac{\partial J_l(u)}{\partial u} + u^2\frac{\partial^2 J_l(u)}{\partial u^2} - l^2 J_l(u)\right)p^2 + u^2 J_l(u)\frac{\partial^2\bar{\Phi}(p,z)}{\partial z^2}\right] = 0. \tag{5.6}$$

The Bessel functions are the solution to the Bessel equation,

$$u^2\frac{\partial^2}{\partial u^2}J_l(u) + u\frac{\partial}{\partial u}J_l(u) + (u^2 - l^2)J_l(u) = 0, \tag{5.7}$$

and from this we see that the term in parentheses is equal to $-u^2 J_l(u)$ and so we get

$$\int_0^\infty dpp J_l(u)u^2\left[\frac{\partial^2}{\partial z^2} - p^2\right]\bar{\Phi}(p,z) = 0, \tag{5.8}$$

and so we must have the $\bar{\Phi}$ fulfilling the condition that

$$\left[\frac{\partial^2}{\partial z^2} - p^2\right]\bar{\Phi}(p,z) = 0. \tag{5.9}$$

This is a second order equation with solutions of exponential form. We will have different coefficients in the two regions, $z > 0$ and $z < 0$,

$$\mathrm{z}{>}\,0 : \bar{\Phi}_>(p,z) = A\mathrm{e}^{pz} + B\mathrm{e}^{-pz} \tag{5.10a}$$

$$\mathrm{z}{<}\,0 : \bar{\Phi}_<(p,z) = C\mathrm{e}^{pz} + D\mathrm{e}^{-pz}. \tag{5.10b}$$

The presence of the grounded plates means that the potential vanishes at $z = \pm h$, which gives us two equations for the coefficients,

$$\begin{aligned} \bar{\Phi}_> \,|_{z=h} = 0 \Leftrightarrow A = -B\mathrm{e}^{-2ph} \\ \Rightarrow \bar{\Phi}_>(p,z) = B\left(\mathrm{e}^{-pz} - \mathrm{e}^{-2ph+pz}\right) \end{aligned} \tag{5.11a}$$

$$\begin{aligned} \bar{\Phi}_< \,|_{z=-h} = 0 \Leftrightarrow C = -D\mathrm{e}^{2ph} \\ \Rightarrow \bar{\Phi}_<(p,z) = D\left(\mathrm{e}^{-pz} - \mathrm{e}^{2ph+pz}\right). \end{aligned} \tag{5.11b}$$

We want the potential to be continuous across the disk, which means that we must have $\bar{\Phi}_>(p,0) = \bar{\Phi}_<(p,0)$, from which it follows that $B = -D\mathrm{e}^{2ph}$ and so

$$\bar{\Phi}_>(p,z) = D\left(\mathrm{e}^{+pz} - \mathrm{e}^{2ph-pz}\right) \tag{5.12a}$$

$$\bar{\Phi}_<(p,z) = D\left(\mathrm{e}^{-pz} - \mathrm{e}^{2ph+pz}\right), \tag{5.12b}$$

which can be written as one expression, the same as (5.12a), but with $z \to |z|$. These we can now insert into the Hankel transformed jump condition, equation (5.2). If we let there be different materials with different dielectric constants on either side of the disk, then taking an average of the dielectric constants $\frac{\epsilon_1+\epsilon_2}{2}$ across the disk gets us

$$D = \frac{4\pi e\bar{n}}{(\epsilon_1+\epsilon_2)p(1+\exp(2hp))}, \tag{5.13}$$

where $\bar{n}$ is the Hankel transform of the radially limited density,

$$\bar{n}(p) = \int_0^\infty drrJ_l(pr)n(r)\Theta(R-r) = \int_0^R drrJ_l(pr)n(r). \tag{5.14}$$

Inserting this in the expression for the potential on either side and setting $z = 0$ gives us the in-plane potential,

$$\bar{\Phi}(p, z=0) = \frac{-4\pi e\bar{n}(p)\tanh(ph)}{p(\epsilon_1+\epsilon_2)}. \tag{5.15}$$

To recover the real-space in-plane potential we just take the inverse transform as described in equation (5.5),

$$\Phi(x) = -\int_0^1 K(x,x')x'N(x'), \tag{5.16}$$

where $x = r/R$ is a dimensionless radial coordinate,

$$N(x) = \frac{4\pi e R \tanh(\frac{h}{R})}{\epsilon_1 + \epsilon_2} n(x), \tag{5.17}$$

and

$$K(x, x') = \coth(\frac{h}{R}) \int_0^\infty dp \tanh(p\frac{h}{R}) J_l(px) J_l(px'). \tag{5.18}$$

This kernel simplifies in either extreme limit of screening. When the screening planes are infinitely far away, i.e. there is no screening, then both hyperbolic tangent and cotangent approach unity, and so we get

$$K_{\text{Unscreened}}(x, x') = \int_0^\infty dp J_l(px) J_l(px'). \tag{5.19}$$

In the case where the screening is absolute we get a local kernel, because $\lim_{h\to 0} \tanh(ph/R) = p/R$ and

$$K_{\text{FullScr}}(x, x') = \int_0^\infty dpp J_l(px) J_l(px') = \frac{1}{x}\delta(x - x'), \tag{5.20}$$

where density and potential become directly proportional for any given x. This result is easy to make sense of, both intuitively and mathematically. Mathematically, h was the vertical distance from the plane where we chose to kill off the potential. Putting this point in the plane means that the potential everywhere is zero except for right on top of the sources of potential, the density. Intuitively, the screening planes affect long-range interactions more strongly than it does close-range interactions. This is because a charge at a point x_0 will see a spatially close charge at a point x_1 with the screening plates (which can be seen as mirror charges $2h$ vertically from the charge at x_1) comparatively far away making the potential felt at point x_0 dominated by the close charge at x_1. On the other hand, it will feel the potential induced induced by a far-away point, x_2, very little, as the screening plates are comparatively close to the plane. Therefore the average charge at x_2 seen by a charge at x_0 will be close the neutral. Letting the screening plates close in on the plane makes x_0 see both x_1 and x_2 as a sandwich of charges and mirror charges, totalling no net charge.

6 Magnetoplasmons in a Discretized Disk

This chapter aims to provide a method with which we can, in a transparent way, apply the boundary condition of letting charge flow into the last site in a numerically solvable way.

We will let the system be set on a lattice, with M sites in the radial direction (radius R), rather than considering a continuous blob. I will presently assume the azimuthal direction to be continuous, so that our lattice is, in fact, a set of concentric rings with edges a distance $\Delta = \frac{R}{M}$ from the edges of the rings immediately inside and outside the given ring. The velocity will dictate flow of charge between rings, see figure 12.

The equations that we will we consider are the two fluid equations, the continuity equation

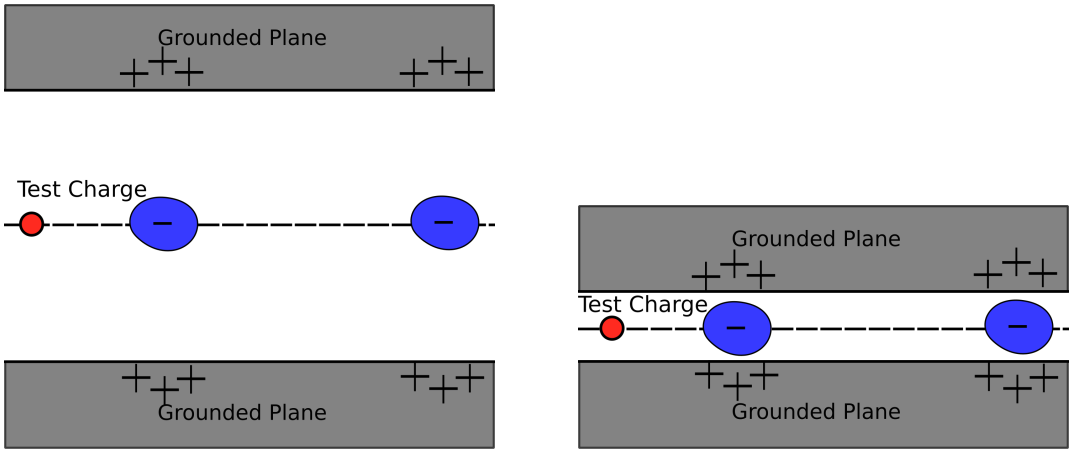

(a) (b)

Figure 11: The effect of screening on the Coulomb interaction. (a) Low screening means that interactions between charges far apart are weaker as all they see is akin to a smeared out charge distribution that, on average, is neutral. (b) When the screening planes approach the disk plane our test charge is barely able to make out the negative charge of the blob closest to it, while the far charge blob is effectively non-existent as seen from the test-charge.

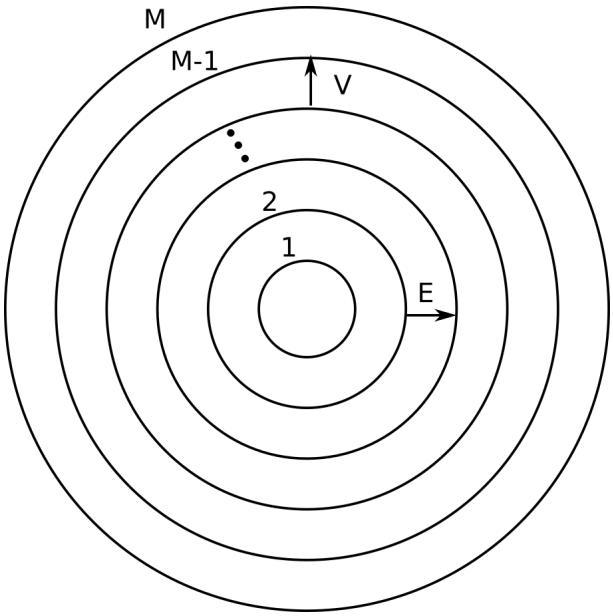

Figure 12: A set of M concentric circles of charged matter. Electric fields are formed and a stream of charged matter (current) runs between each consecutive ring.

$$-i\omega n + n_0 \nabla \cdot \vec{v} = 0, \tag{6.1}$$

and the Euler equation,

$$-i\omega \vec{v} - \frac{e}{m}\nabla\Phi - \omega_c \hat{z} \times \vec{v} = 0, \tag{6.2}$$

where we have omitted the term proportional to the compressional wave velocity, s. This can readily be done when in the long wave-length limit where $\frac{s^2}{R^2}$ is negligible compared to the bulk frequency.

We can consider each component of the vector equation (6.2) and isolate and eliminate the azimuthal component of the velocity (this was continuous, so we can do this before discretizing). From the first component we get

$$\begin{aligned} -i\omega v_r - \frac{e}{m}\partial_r\Phi + \omega_c v_\theta = 0 \\ \Leftrightarrow v_r = \frac{i}{\omega}\left[\frac{e}{m}\partial_r\Phi - \omega_c v_\theta\right]. \end{aligned} \tag{6.3}$$

The second component gives us

$$\begin{aligned} -i\omega v_\theta - \frac{iel}{mr}\Phi - \omega_c v_r = 0 \\ \Leftrightarrow v_\theta = \frac{i}{\omega}\left[\frac{iel}{mr}\Phi + \omega_c v_r\right]. \end{aligned} \tag{6.4}$$

If we then insert this into the equation for the first (radial) component we get an equation containing only n, Φ, and v_r, (the angular dependence of all our quantities are assumed to be of the form $\exp(il\theta)$),

$$v_r = \frac{i}{\omega^2 - \omega_c^2}\left[\omega\partial_r + \frac{l\omega_c}{r}\right]\frac{e}{m}\Phi, \tag{6.5}$$

after multiplying through by ω^2.

We can also insert our expression for v_θ into the continuity equation, (6.1),

$$\begin{aligned} -i\omega n + n_0\nabla\cdot\vec{v} = -i\omega n + n_0\left[\partial_r v_r + \frac{v_r}{r} + \frac{il}{r}v_\phi\right] \\ = -i\omega n + n_0\left[\partial_r v_r + \frac{v_r}{r} - \frac{l}{r\omega}\left(\frac{iel}{mr}\Phi + \omega_c v_r\right)\right] = 0. \end{aligned} \tag{6.6}$$

From here on out, we will drop the r-index on the radial velocity; since the azimuthal velocity has now been eliminated there will be no confusion and it will be less crowded when we start adding site indices.

The, perhaps, most natural way to think of the flow of charge along the radial direction is through the velocity that lives inbetween the sites, describing the flow from site j to site $j+1$,

$v_{j,j+1}$.[2] These offset "sites" need to be treated in a way so that they can be compared to the quantities that live on the previously constructed sites, as needed for the Lorentz force. This we will do by connecting the velocity at a given site with the average of the velocities going into the site and out of the site, with positive velocity going from the center of the disk to the edge. In this way, the velocity at site j will be

$$v_j = \frac{v_{j-1,j} + v_{j,j+1}}{2}. \tag{6.7}$$

It is natural to think of the potential as living on the sites since the potential is generated by the charge density living on the site. The velocity and the radial derivative of the potential are most naturally defined as living on the bonds between sites. Such a bond-derivative will be done with the standard discretized form of the derivative, $\frac{\partial}{\partial r} q|_{j,j+1} = \frac{q_{j+1} - q_j}{\Delta}$. Equation (6.5) therefore has a quantity living on the bonds between sites on the LHS and a quantity living on the bonds (derivative of potential) and one living on-site (potential) on the RHS. For this reason we will make use of averages when we mix bond and on-site terms, so that for a point in the bulk, $j \neq M$, we will have

$$v_{j,j+1} = i\frac{e}{m}\frac{1}{\omega^2 - \omega_c^2}\left(\omega\frac{\Phi_{j+1} - \Phi_j}{\Delta} + \frac{l\omega_c}{2}\left(\frac{\Phi_{j+1}}{r_{j+1}} + \frac{\Phi_j}{r_j}\right)\right), \tag{6.8}$$

and, using equations (6.8) and (6.7) we can get an expression for the on-site velocity,

$$v_j = \frac{v_{j-1,j} + v_{j,j+1}}{2} = i\frac{e}{m}\frac{1}{\omega^2 - \omega_c^2}\left[\omega\frac{\Phi_{j+1} - \Phi_{j-1}}{2\Delta} + \frac{l\omega_c}{4}\left(\frac{\Phi_{j+1}}{r_{j+1}} + 2\frac{\Phi_j}{r_j} + \frac{\Phi_{j-1}}{r_{j-1}}\right)\right]. \tag{6.9}$$

Although it is not needed quite yet, for consistency we will take a natural candidate for differentiation of an on-site quantity Q at site j to be

$$\frac{\partial}{\partial r} Q_i = \frac{Q_{i+1} - Q_{i-1}}{2\Delta}, \tag{6.10}$$

while the onsite velocity derivative will be taken to be the difference between flow into and out of a site,

$$\frac{\partial v_j}{\partial r} = \frac{v_{j,j+1} - v_{j-1,j}}{\Delta} = i\frac{e}{m}\frac{1}{\omega^2 - \omega_c^2}\left[\omega\frac{\Phi_{j+1} - 2\Phi_j + \Phi_{j-1}}{\Delta^2} + \frac{l\omega_c}{2\Delta}\left(\frac{\Phi_{j+1}}{r_{j+1}} - \frac{\Phi_{j-1}}{r_{j-1}}\right)\right]. \tag{6.11}$$

We see that, although we did not impose it directly, the term in parentheses in equation (6.11) is already on the form of equation (6.10).

Inserting equations (7.14) and (6.11) into equation (6.6) gives

[2] When a velocity appears with a site index it is implicit that it is velocity in the radial direction, as we treat the angular direction continuously and not discretely.

$$
\begin{aligned}
0 = -i\omega n_j + n_0 \left(\frac{v_{j,j+1} - v_{j-1,j}}{\Delta} + \left(\frac{1}{r_j} - \frac{l\omega_c}{r_j\omega}\right) v_j \right) - \frac{in_0 el^2}{\omega m r_j^2}\Phi_j \Leftrightarrow \\
-i\omega n_j + i\frac{n_0 e}{m}\frac{1}{\omega^2-\omega_c^2}\left[\left(\omega\frac{\Phi_{j+1}-2\Phi_j+\Phi_{j-1}}{\Delta^2} + \frac{l\omega_c}{2\Delta}\left(\frac{\Phi_{j+1}}{r_{j+1}} - \frac{\Phi_{j-1}}{r_{j-1}}\right)\right)\right] \\
+i\frac{n_0 e}{r_j m}\frac{1}{\omega^2-\omega_c^2}\left(1-\frac{l\omega_c}{\omega}\right)\left[\omega\frac{\Phi_{j+1}-\Phi_{j-1}}{2\Delta} + \frac{l\omega_c}{4}\left(\frac{\Phi_{j+1}}{r_{j+1}} + 2\frac{\Phi_j}{r_j} + \frac{\Phi_{j-1}}{r_{j-1}}\right)\right] \\
- \frac{in_0 el^2}{\omega m r_j^2}\Phi_j = 0
\end{aligned}
\tag{6.12}
$$

Multiplying the above equation by $-i(\omega^2-\omega_c^2)\frac{4\pi eR\tanh(h/R)}{1+\epsilon}$ and using our dimensionless radial coordinates, $x = r/R$ and $dx = \Delta/r$, we can rewrite it slightly to

$$
\begin{aligned}
-(\omega^2-\omega_c^2)\omega N_j + \Omega_0^2\left[\left(\omega\frac{\Phi_{j+1}-2\Phi_j+\Phi_{j-1}}{dx^2} + \frac{l\omega_c}{2dx}\left(\frac{\Phi_{j+1}}{x_{j+1}} - \frac{\Phi_{j-1}}{x_{j-1}}\right)\right)\right] \\
+\frac{1}{x_j}\Omega_0^2\left(1-\frac{l\omega_c}{\omega}\right)\left[\omega\frac{\Phi_{j+1}-\Phi_{j-1}}{2dx} + \frac{l\omega_c}{4}\left(\frac{\Phi_{j+1}}{x_{j+1}} + 2\frac{\Phi_j}{x_j} + \frac{\Phi_{j-1}}{x_{j-1}}\right)\right] \\
- (\omega^2-\omega_c^2)\frac{\Omega_0^2 l^2}{\omega x_j^2}\Phi_j = 0,
\end{aligned}
\tag{6.13}
$$

where $N_j = \frac{4\pi eR\tanh(h/R)}{1+\epsilon}n_j$, $\Omega_0^2 = \frac{4\pi e^2 n_0\tanh(h/R)}{mR(1+\epsilon)}$ and the connection between particle density and electromagnetic potential is given by equations (5.16)-(5.18).

6.1 On the Edge

It is on the edge that we want to impose our boundary condition, disallowing flow out of the last site, $v_{M,M+1} = 0$. To do this we can just adjust equation (6.13) for the last site to reflect this change. Certain averages and derivatives will now look different. Setting these "beyond-the-edge" terms to 0 gives

$$
\begin{aligned}
-(\omega^2-\omega_c^2)\omega N_M + \Omega_0^2\left[\omega\frac{-\Phi_M+\Phi_{M-1}}{dx^2} - \frac{l\omega_c}{2dx}\left(\frac{\Phi_M}{x_M} + \frac{\Phi_{M-1}}{x_{M-1}}\right)\right] \\
+\frac{1}{x_M}\Omega_0^2\left(1-\frac{l\omega_c}{\omega}\right)\left[\omega\frac{\Phi_M-\Phi_{M-1}}{2dx} + \frac{l\omega_c}{4}\left(\frac{\Phi_M}{x_M} + \frac{\Phi_{M-1}}{x_{M-1}}\right)\right] \\
- (\omega^2-\omega_c^2)\frac{\Omega_0^2 l^2}{\omega x_j^2}\Phi_j = 0.
\end{aligned}
\tag{6.14}
$$

Equations (6.13) and (6.14) together with equations (5.16) and (5.18) show the behaviour of single components of the density "potential", N, as a homogeneous eigenvalue equation, $\underline{\underline{\mathbf{A}}}\cdot\underline{\mathbf{N}} = 0$. The allowed modes are those that ensure that the determinant of the combined matrix, $\underline{\underline{\mathbf{A}}}$, vanishes. These modes have an associated eigenvector, $\underline{\mathbf{N}}$, that describes the density potential, as given by equation (5.17), at every site. When solving for the eigenvectors of equations (6.13) and (6.14) for different parameters we risk getting different global phases. For that reason it is not educational to compare a difference in sign between cases. Rather, it is the relative shape

of the edge mode that is of interest.

Before we can proceed to the numerical solution for the plasmon modes, we need to discretize the kernel of the potential-density relation.

6.2 Discretization of the Kernel

As is to be expected for the Coulomb interaction, $k(x, x')$ blows up when $x' \to x$, i. e. when two charged density elements lie on top of each other. To circumvent this in the numerical calculation, we use a smearing procedure; each small discretized density element does not correspond to a single electron, but rather a distribution of electrons withing the element, and electrons interacting within the same density element would correspond to $x = x'$. For that reason we will approximate the "diagonal" parts of the kernel by assuming that the "density", $N(x')$, does not change drastically for values of x' in a small region close to x as compared to the kernel. The diagonal will be assigned an averaged value across the soft divergence (integrating across the divergence yields a finite value),

$$\tilde{K}(x' = x) = \frac{1}{dx} \int_{-\frac{dx}{2}}^{\frac{dx}{2}} d(\Delta x)\, K(\bar{x}, \Delta x), \tag{6.15}$$

where $\bar{x} = \frac{x+x'}{2}$, $\Delta x = x - x'$, and $dx = \frac{1}{M}$ is the grid-spacing.

This approach works wonderfully when considering the two cases of extreme screening, but when considering arbitrary screening it may be necessary to employ the well-known asymptotic behaviour of the Bessel functions of the first kind to separate the p-integral in two parts,

$$\begin{aligned} K(x, x') = K_{body}(x, x') + K_{tail}(x, x') = \coth(\frac{h}{R}) \int_0^C dp \tanh(p\frac{h}{R}) J_l(px) J_l(px') \\ + \coth(\frac{h}{R}) \int_C^\infty dp \tanh(p\frac{h}{R}) \left[\sqrt{\frac{2}{\pi px}} \cos(px - L\pi/2 - \pi/4) \sqrt{\frac{2}{\pi px'}} \cos(px' - L\pi/2 - \pi/4) \right], \end{aligned} \tag{6.16}$$

where C is an appropriate cut-off, such that the asymptotic behaviour of the Bessel functions has set in and the substitution is valid. Expressing K_{tail} in terms of $\bar{x}$ and Δx simplifies the expression greatly,

$$K_{tail}(\bar{x}, \Delta x) = \coth(\frac{h}{R}) \int_0^C dp \tanh(p\frac{h}{R}) \left(p\pi \sqrt{\bar{x}^2 - \frac{\Delta x^2}{4}} \right)^{-1} \left[\cos(p\Delta x) + \cos(2p\bar{x} - L\pi - \frac{\pi}{2}) \right]. \tag{6.17}$$

In all numerical computations using this cut-off method the cutoff has been set at $C = 2 \cdot 10^5$.

6.3 Relation to the Case of the Infinite Half-Plane

Although the two cases are different it is still possible to draw parallels between the results for the infinite half-plane and the disk. During the discussion above we have assumed that the disk has an angular symmetry such that $f(\mathbf{r}) = f(r)\mathrm{e}^{il\theta}$ which results in the angular derivative always being of the form $\frac{1}{r}\frac{\partial}{\partial\theta} \to \frac{il}{r}$. The $\frac{1}{r}$ comes naturally from the cylindrical nature of our coordinate system but is not part of the actual derivative. In the case of the infinite half-plane we considered a system in which we had a translational symmetry along the y-direction, each point along the y-axis differing only from the next by a phase $\mathrm{e}^{iq\Delta y}$, resulting in the spatial derivative along the y-direction to be of the form $\frac{\partial}{\partial y} \to iq$.

Conceptually one can imagine that a very large disk, as compared to the wavelength, so large that there is no appreciable curvature to the edge during a full wavelength of the mode, would exhibit behaviour similar to that of an infinite half-plane. This corresponds to modes with large angular momenta.
The angle θ goes from 0 to 2π as we go around the perimeter of the disk. The circumference of a disk of radius R is $2\pi R$, and so we can imagine that if we were to map the half-plane to the disk using y as the coordinate around the perimeter of the disk, we could use the small angle approach (a full wavelength on a very large disk traces out a small angle), $\sin(\theta) = \sin(\frac{y}{R}) \approx \frac{y}{R}$. This goes from 0 to 2π as we go all the way around the disk (y goes from 0 to $2\pi R$), just as θ does.

Both phases, $l\theta$ and qy, go from 0 to $2\pi \times$ integer depending on how many wavelengths we sweep out. From the discussion above we can now make the rough estimation that $l\theta \approx l(\frac{y}{R}) \approx qy$ for large l, such that $l \approx qR$.

Alternatively, one can just compare the wavelengths of the two systems; on the half-plane, the wavelength is $\lambda_{plane} = \frac{2\pi}{q}$ and on the disk it the circumeference of the disk divided by the number of wavelengths we fit on it, $\lambda_{disk} = \frac{2\pi R}{l}$, which means that we will have $q \approx \frac{l}{R}$. This comparison is most accurate when $\frac{\lambda_{disk}}{R} << 1$.

6.4 Results for the Magnetoplasmon - Density Profile, 3D Profile and Dispersion

We will in general use $M = 160$ sites, meaning we have modelled the disk as consisting of 160 concentric rings. From this we can find the ground state modes, going either way around the disk, and see how they evolve with increasing angular momentum. Writing all frequencies in units of the bulk frequency, Ω_0, we see in figure 13a that in the limit of no magnetic field the dispersion for large l has a shape similar to that of the half-plane, $\omega_\pm = \sqrt{\frac{2l}{3}}\Omega_0$, as predicted by equation 4.13 , where we have let $\Omega_q \to \sqrt{l}\Omega_0$, as argued in chapter 6.3 above, though there is a discrepancy between the results. This discrepancy is discussed in chapter 7.4, where it is argued that the cause may be the difference between using the local kernel approximation and the exact kernel.

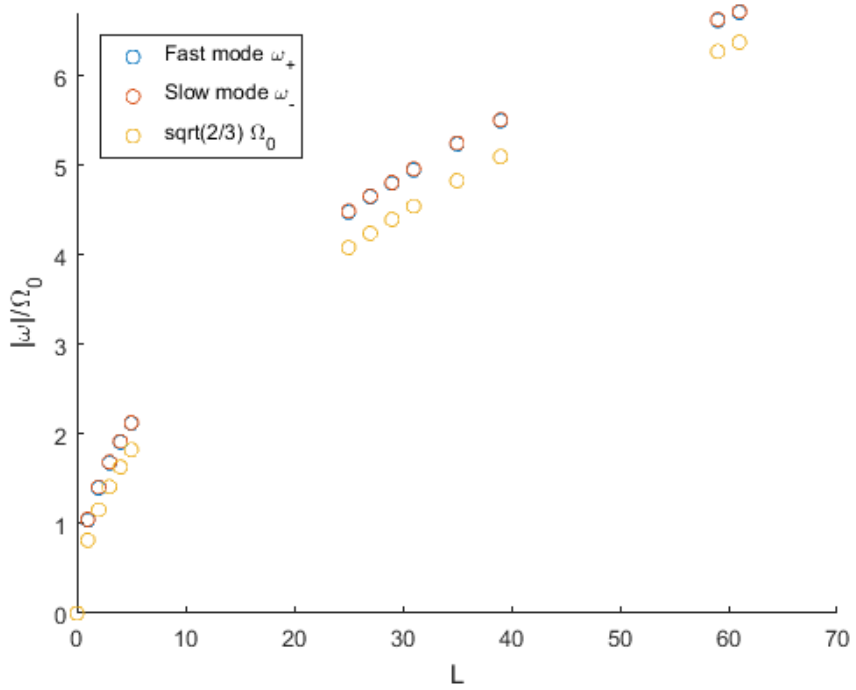

(a) The zero-field ($\omega_c = 0$) dispersion of the now degenerate groundstate, along with the line showing $\omega/\Omega_0 = \sqrt{\frac{2}{3}L}$. Note that the plot points of the two modes overlap because of this degeneracy.

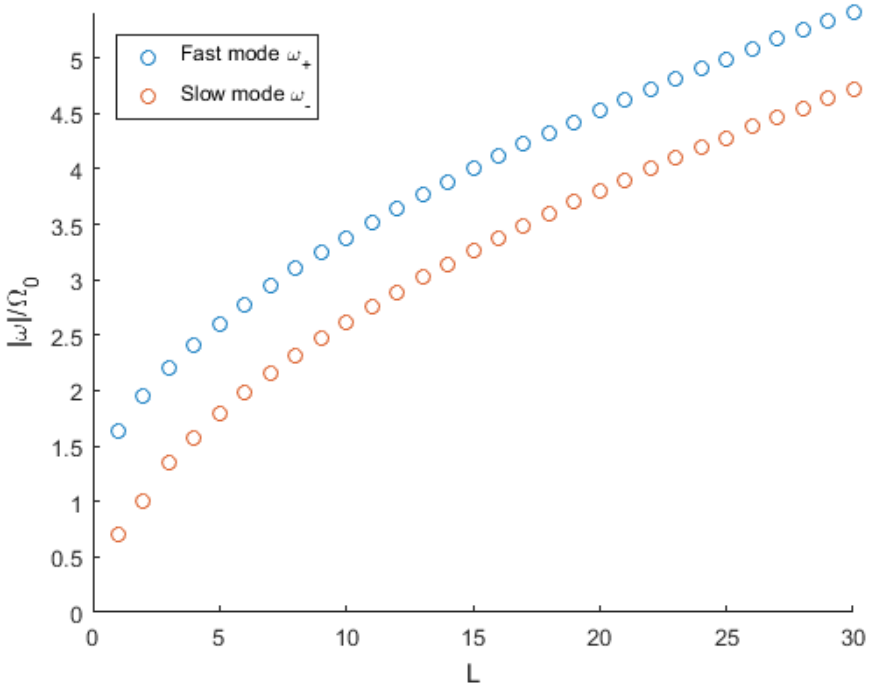

(b) The ground state energies of the two counterdirectional modes, ω_+ and ω_- for different angular momenta at a magnetic field corresponding to $\omega_c/\Omega_0 = 1$.

Figure 13: The dispersion of the ground state of the two modes in different cases, plotted against the abolute value of the angular momentum, $L = |l|$.

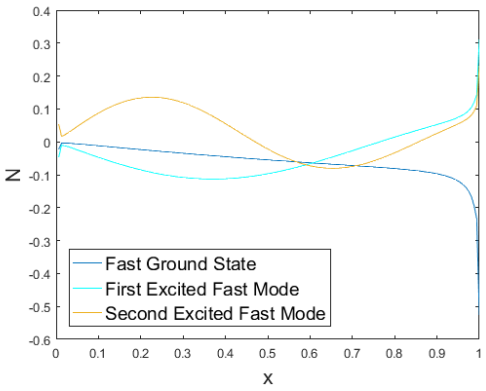

(a) Density profile for $l = 1$.

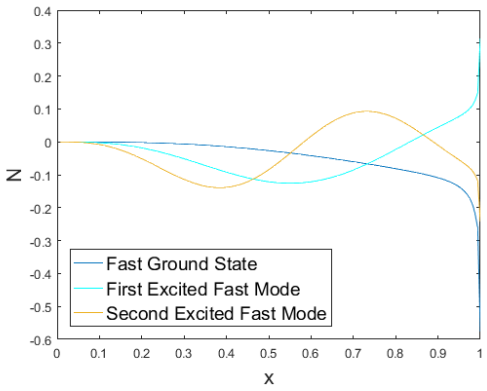

(b) Density profile for $l = 3$.

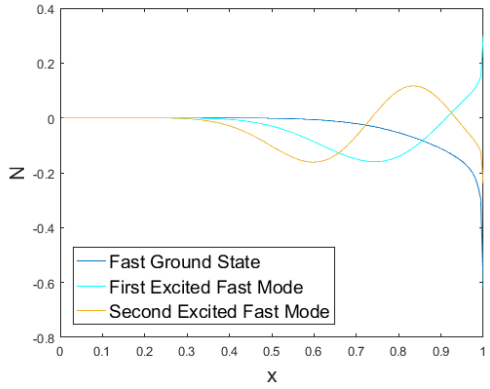

(c) Density profile for $l = 10$.

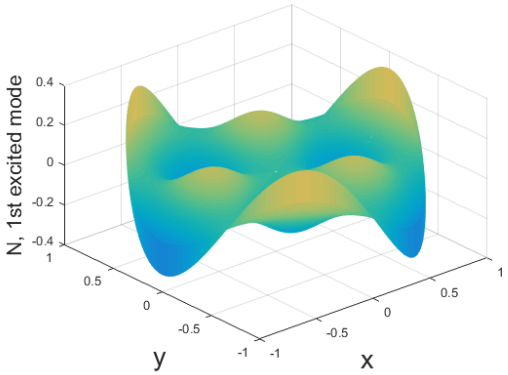

(d) 3D plot of the density for the first excited plus mode for $l = 3$.

Figure 14: (a)-(c):The density profiles for the three lowest plus modes for (a) $l = 1$, (b) $l = 3$ and (c) $l = 10$ at $\frac{\omega_c}{\Omega_0} = 2$.Note that the first two points are off in (a). This may be due to the potential being linear at small x for $l = 1$ (this is described in more detail in chapter 7.2). (d) 3D plot of the density of the first excited plus mode with $l = 3$, $\frac{\omega_c}{\Omega_0} = 2$. All frequencies are measured in units of Ω_0.

Turning on the magnetic field, we get for $\omega_c/\Omega_0 = 1$ and no screening, $h/R = 0$, the evolution seen in figure 13b. We see that the splitting, the chirality, of the ground state stays somewhat constant (although slightly decreasing) with increasing angular momentum. For $\omega_c = \Omega_0$ and the lowest angular momentum considered, $l = 1$, we get the splitting to be $\Delta\omega = \omega_+ - \text{abs}(\omega_-) = 0.92\Omega_0$. Comparing this to the result from the infinite half-plane gives, as predicted by equations (4.11a) and (4.11b) with $\omega_c = \Omega_0$, $\Delta\omega = \frac{2\sqrt{2}}{3}\omega_c \approx 0.94\Omega_0$. Qualitatively this looks quite similar to what we might expect but the decreasing splitting may be another consequence stemming from the use of the exact kernel as opposed to the approximate kernel that was used to derive the result in equations (4.11a) and (4.11b).

Figure 14 gives an overview of the evolution of the density near the edge as we go to higher angular momenta and higher modes of excitation for $\frac{\omega_c}{\Omega_0} = 2$. Examining the density profiles of the few lowest modes we see that increasing the angular momentum, aside from just fitting in l

full wavelengths around the perimeter of the disk, pushes the mode toward the edge, decreasing the decay length and thereby increasing the confinement. This is to be expected based on the x-dependence of the potential of the modes of the half-space and half-plane of chapters 3.4 and 4, for example through equation (3.16), and the connection between l and q as discused in chapter 6.3. Along the same lines, higher modes tend to delocalize the state, increasing the amplitude toward the center of the disk. Each higher mode needs to fit in an additional node, so that for a mode n, with $n = 1$ being the ground state, there are $n - 1$ nodes in the density in the radial direction. Figure 14d shows how a snapshot of the density field of the entire disk looks for the first excitation above the ground state of the $l = 3$ mode. Note that the nodal points stay nodes all the way around the disk. It is important to note the shortcomings of the model however, because a resolution of 160 radial points may not be conducive to an examination of cases where $l \approx 50 - 60$. When approaching angular momenta so large that the density changes rapidly near the edge because of the stricter confinement, for example when considering a highly excited mode at large angular momentum, one has to make sure that the resolution used is dense enough to reflect this.

The main topic of this paper will be a different kind of plasmons, the framework for which will be introduced below.

7 Anomalous Berry Plasmons in Disk Geometry

When you have a material with non-zero Berry curvature it is possible to realize edge states similar to those of the magnetoplasmons, due to the transverse nature of the anomalous velocity. If the material is two-dimensional and the parameter from which we get the curvature is momentum, then the Berry curvature vector, as given by equation (2.14), points out of plane, enabling us to realize an anomalous Hall system with the charge pushed to the edge forming a collective excitation. The shifting positive and negative net charge along the edge causes electric fields to form orthogonal to the equipotential lines, and so parallel to the edge, which in turn causes shifting orthogonal anomalous velocity into or out of the edge. The result is that the negative charge at the "tail" of one wavefront jumps back to the front of the one behind it (see figure 15), or vice versa, causing the wave propagation to speed up or slow down, respectively. This chiral behaviour arises from the front of the wavefront "sucking" in charge from the tail ends of the nearest adjacent wavefronts, so to speak. In this chapter we will try to establish the basic framework for these collective excitations on a disk.

7.1 The system

The system to be examined here is, like that for the magnetoplasmon, that of a two dimensional disk of charged particle-soup on a grid of oppositely charged background, with angular symmetry (such that a spatially dependent quantity f will be of the form $f(\vec{r}) = f(r)\exp(il\theta)$). The electron density is the sum of the unperturbed density, n_0, and the perturbation, denoted n.

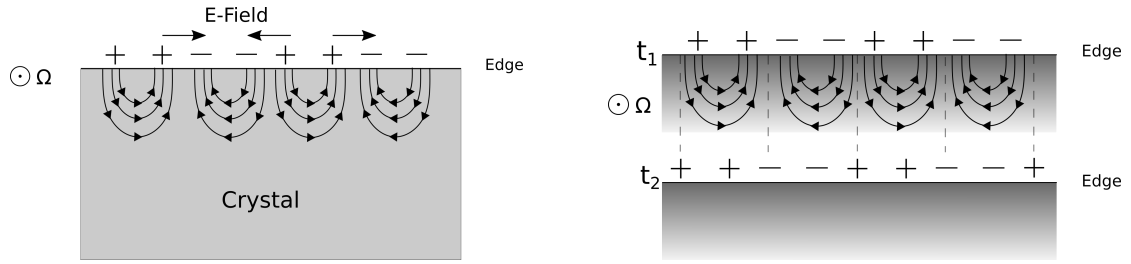

(a) (b)

Figure 15: The workings behind the "up-stream" and "downstream" directions caused by the presence of outward pointing Berry curvature and the resulting anomalous velocity. The anomalous velocity is parallel to the equipotential lines and the direction is given by the arrows. The movement of negatively charged density elements causes the wavefronts to move to the left, making the left moving mode flow downstream (faster) and the right-moving mode flow up-stream (slower). (a) The workings of the anomalous contribution to the propagation of plasmon modes in relation to the crystal. (b) 2 snapshots of the wave fronts at times t_1 and t_2 ($t_2 > t_1$).

The solutions that we search for will be steady-state solutions (all transient behaviour will be gone), such that our two governing equations for individual conduction band electrons, the continuity equation and the Euler (force) equation, can be written as

$$-i\omega n + n_0 \nabla \cdot \mathbf{v} = 0 \Leftrightarrow \tag{7.1}$$

and

$$-i\omega \frac{\mathbf{p}}{m} - \frac{e}{m}\nabla\Phi = 0. \tag{7.2}$$

In our model we will not be considering the motion of individual electrons. Instead we will be concerned with the associated density fields, denoted by a bar, $\overline{Q}$. Such a density field is gotten by integrating across the phase space density, $f(\mathbf{r}, \mathbf{p}, t)$, so that

$$\overline{Q} = \sum_i \int d^2\mathbf{p} Q(\mathbf{r}, \mathbf{p}) f_i(\mathbf{r}, \mathbf{p}, t)/(2\pi\hbar)^2, \tag{7.3}$$

where i runs over the different energy bands.

Because of the nature of the anomalous velocity we also have take into account the electron transport of the valence band, as seen in the example of the one-dimensional insulator. If the chemical potential lies in the lower part of the conduction band we will have some conventional current from the conduction electrons and some anomalous current from both the valence and conductance electrons (this will only make a small contribution and if we only have those two bands it will have opposite sign because the Berry curvature summed over all bands is zero). The associated equations for the density fields are

$$\begin{aligned} -i\omega n + \nabla \cdot \overline{\mathbf{v}} = 0 \Leftrightarrow \\ -i\omega n + \left[\frac{1}{r}\overline{v}_r + \frac{\partial}{\partial r}\overline{v}_r + \frac{il}{r}\overline{v}_\theta\right] = 0 \end{aligned} \tag{7.4}$$

and

$$-i\omega\frac{\overline{\mathbf{p}}}{m} - (n_0 + n)\frac{e}{m}\nabla\Phi = 0, \tag{7.5}$$

where $\overline{\mathbf{v}}$ and $\overline{\mathbf{p}}$ are the velocity and momentum density fields, respectively.

We only want to consider the first order corrections, so terms like $n\nabla\Phi$ will be discarded as they are second order in the perturbation.

We can write the components of equation (7.5) individually to get expressions for the components of the momentum. The radial component gives

$$\begin{aligned} -i\omega\frac{\overline{p}_r}{m} - n_0\frac{e}{m}\frac{\partial}{\partial r}\Phi = 0 \Leftrightarrow \\ \frac{\overline{p}_r}{m} = i\frac{n_0 e}{m\omega}\frac{\partial}{\partial r}\Phi \end{aligned} \tag{7.6}$$

while the angular component gives us

$$\begin{aligned} -i\omega\frac{\overline{p}_\theta}{m} - n_0\frac{eil}{mr}\Phi = 0 \Leftrightarrow \\ \frac{\overline{p}_\theta}{m} = -\frac{n_0 el}{m\omega r}\Phi. \end{aligned} \tag{7.7}$$

Given the presence of non-zero Berry curvature in our material, we get anomalous terms that are just the combinations of equations (2.36) and (7.3),

$$\overline{\mathbf{v}}_a = \frac{e\mathcal{F}}{\hbar}\nabla\Phi \times \hat{z}, \tag{7.8}$$

with $\mathcal{F} = \sum_i \int d^2\mathbf{p}\boldsymbol{\Omega}(\mathbf{p}) f_i(\mathbf{r}, \mathbf{p}, t)/(2\pi\hbar)^2$ (called the Berry flux) and we have assumed that $\frac{1}{\hbar}\frac{\partial\epsilon_n(k)}{\partial k} = \frac{p}{m}$. Since $\mathcal{F}$ always appears accompanied by the induced electric field, $\nabla\Phi$, the first order contribution comes from the equilibrium phase space density, f_i^0.

The individual components of the velocity field are of the form

$$\overline{v}_\theta = \frac{\overline{p}_\theta}{m} + \overline{v}_{a,\theta} = -\frac{n_0 el}{m\omega r}\Phi - \frac{e\mathcal{F}}{\hbar}\frac{\partial}{\partial r}\Phi \tag{7.9}$$

and

$$\overline{v}_r = \frac{\overline{p}_r}{m} + \overline{v}_{a,r} = i\frac{n_0 e}{m\omega}\frac{\partial}{\partial r}\Phi + \frac{ile\mathcal{F}}{\hbar r}\Phi, \tag{7.10}$$

where, again, we have assumed that $\frac{1}{\hbar}\frac{\partial\epsilon_n(k)}{\partial k} = \frac{p}{m}$.

Straight insertion of these into equation (7.4) shows that the anomalous velocity has no effect on the bulk of the material where there are no edges to be concerned about. This is because

the continuity equation is concerned only with the relation between what runs into and what runs out of a given point. Adding a term to the velocity that contains the transverse electric field (derivative of the potential in the direction normal to the component in question) does not cause a pile-up in the bulk. It *can*, however, cause a pileup at the edge.

Inserting equation (7.9) into equation (7.4) gives us an equation containing only quantitites that we intend to discretize,

$$-i\omega n + \left[\frac{1}{r}\overline{v}_r + \frac{\partial}{\partial r}\overline{v}_r + \frac{il}{r}\overline{v}_\theta\right] = -i\omega n + \frac{\overline{v}_r}{r} + \frac{\partial \overline{v}_r}{\partial r} - i\frac{l^2 n_0 e}{m\omega r^2}\Phi - i\frac{le\mathcal{F}}{\hbar r}\frac{\partial}{\partial r}\Phi = 0. \tag{7.11}$$

7.2 Discretization of the Berry Plasmon

The discretization procedure will resemble that of the discretization of the magnetoplasmon case, so we will merely make a summary of the points to consider.

We treated the azimuthal direction continuously, eliminating all angular components of the velocity, v_θ, in equation (7.11) above, which is the equation that we wish to discretize. We cut the disk, of radius R, up into M concentric rings (labelled with an index j), with neightbouring rings spaced a distance $\Delta = R/M$ apart. We picture certain quantities living on the sites. These are the density, n_j and the potential induced by the density, Φ_j. On the bonds between the sites live the electric field, proportional to the radial derivative of the induced potential, and the radial velocity flowing into site j from site $j-1$, $v_{j-1,j}$.

Equation (7.11) consists of quantities both on-site and on the bonds. Therefore we need to evaluate on-site versions of the velocity by taking averages of the flow into and out of the site using equation (6.7). Equation (7.10) has the velocity living on the bonds between sites on the LHS and the potential and its derivative on the RHS. We will again make use of averages of the on-site potential when considering the bond velocity. When considering the derivative of the potential on a given site j, then we will be using equation (6.10), such that

$$\frac{\partial \Phi_j}{\partial r} = \frac{\Phi_{j+1} - \Phi_{j-1}}{2\Delta}. \tag{7.12}$$

Finally we want to impose the boundary condition that current is allowed to run into the last site, but not out of the disk, so that $v_{M,M+1} = 0$.

Starting from equation (7.10) and averaging the potential, the bond velocity flowing from site j into site $j+1$ becomes

$$\overline{v}_{j,j+1} = i\frac{n_0 e}{mw}\frac{\Phi_{j+1} - \Phi_j}{\Delta} + i\frac{el\mathcal{F}}{2\hbar}\left(\frac{\Phi_{j+1}}{r_{j+1}} + \frac{\Phi_j}{r_j}\right). \tag{7.13}$$

The on-site velocity at site j can be determined using equation (6.7),

$$\overline{v}_j = \frac{\overline{v}_{j,j+1} + \overline{v}_{j-1,j}}{2} = i\frac{n_0 e}{m\omega}\frac{(\Phi_{j+1} - \Phi_{j-1})}{2\Delta} + i\frac{el\mathcal{F}}{4\hbar}\left(\frac{\Phi_{j+1}}{r_{j+1}} + 2\frac{\Phi_j}{r_j} + \frac{\Phi_{j-1}}{r_{j-1}}\right). \tag{7.14}$$

and the on-site derivative can be found just as in equation (6.11),

$$\frac{d\overline{v}_j}{dr} = i\frac{n_0 e}{m\omega\Delta^2}\left(\Phi_{j+1} - 2\Phi_j + \Phi_{j-1}\right) + i\frac{el\mathcal{F}}{\hbar}\left(\frac{\Phi_{j+1}}{r_{j+1}} - \frac{\Phi_{j+1}}{r_{j-1}}\right). \tag{7.15}$$

Now we have all the ingredients for equation (7.11) and putting all together gives us an equation valid in the bulk,

$$\begin{aligned} -\omega n_j + \frac{n_0 e}{m\omega}\frac{\Phi_{j+1} - \Phi_{j-1}}{2\Delta r_j} + \frac{el\mathcal{F}}{4\hbar r_j}\left(\frac{\Phi_{j+1}}{r_{j+1}} + 2\frac{\Phi_j}{r_j} + \frac{\Phi_{j-1}}{r_{j-1}}\right) \\ + \frac{n_0 e}{m\omega\Delta^2}\left(\Phi_{j+1} - 2\Phi_j + \Phi_{j-1}\right) + \frac{el\mathcal{F}}{2\hbar\Delta}\left(\frac{\Phi_{j+1}}{r_{j+1}} - \frac{\Phi_{j-1}}{r_{j-1}}\right) \\ - \frac{l^2 n_0 e}{m\omega r_j^2}\Phi_j - \frac{el\mathcal{F}}{\hbar r_j}\frac{\Phi_{j+1} - \Phi_{j-1}}{2\Delta} = 0. \end{aligned} \tag{7.16}$$

For large r (that is not on the edge) we see that the anomalous part vanishes. This is so because when $r_j/\Delta >> 1$ we have

$$\frac{el\mathcal{F}}{4\hbar r_j}\left(\frac{\Phi_{j+1}}{r_{j+1}} + 2\frac{\Phi_j}{r_j} + \frac{\Phi_{j-1}}{r_{j-1}}\right) \approx \frac{el\mathcal{F}}{\hbar r_j^2}\Phi_j, \tag{7.17}$$

and

$$\begin{aligned} \frac{el\mathcal{F}}{2\hbar\Delta}\left(\frac{\Phi_{j+1}}{r_{j+1}} - \frac{\Phi_{j-1}}{r_{j-1}}\right) &= \frac{el\mathcal{F}}{2\hbar\Delta}\left(\frac{r_j(\Phi_{j+1} - \Phi_{j-1}) - \Delta(\Phi_{j+1} + \Phi_{j-1})}{r_j^2 - \Delta^2}\right) \\ \approx \frac{el\mathcal{F}}{\hbar}\left(\frac{\Phi_{j+1} - \Phi_{j-1}}{2\Delta r_j} - \frac{\Phi_{j+1} + \Phi_{j-1}}{2r_j^2}\right) &\approx \frac{el\mathcal{F}}{\hbar}\left(\frac{\Phi_{j+1} - \Phi_{j-1}}{2\Delta r_j} - \frac{\Phi_j}{r_j^2}\right), \end{aligned} \tag{7.18}$$

which causes all terms proportional to $\mathcal{F}$ to vanish.

Now we want to let $v_{M,M+1} = 0$ and evaluate equation (7.11) on site M. Combining all our ingredients with the above condition gives us an equation valid on the edge,

$$\begin{aligned} -\omega n_M + \frac{n_0 e}{m\omega}\frac{\Phi_M - \Phi_{M-1}}{2\Delta r_M} + \frac{el\mathcal{F}}{4\hbar r_M}\left(\frac{\Phi_M}{r_M} + \frac{\Phi_{M-1}}{r_{M-1}}\right) + \frac{n_0 e}{m\omega\Delta^2}\left(-\Phi_M + \Phi_{M-1}\right) \\ + \frac{el\mathcal{F}}{2\hbar\Delta}\left(-\frac{\Phi_M}{r_M} - \frac{\Phi_{M-1}}{r_{M-1}}\right) - \frac{n_0 e l^2}{m\omega r_M^2}\Phi_M - \frac{el\mathcal{F}}{\hbar r_M}\left(\frac{\Phi_{M+1} - \Phi_{M-1}}{2\Delta}\right) = 0, \end{aligned} \tag{7.19}$$

where $r_M = R$, but we have kept the subscript for clarity and ease of transition between the expressions.

Multiplying through by $\frac{4\pi e R\tanh(h/R)}{1+\epsilon}$ (and ω) and introducing the dimensionless radial coordinate, $x = \frac{r}{R}$, the density with dimensions of potential, N, and the frequency Ω_0, where

$$N_j = \frac{4\pi e R\tanh(h/R)}{1+\epsilon} n_j, \tag{7.20}$$

$$\Omega_0^2 = \frac{4\pi e^2 n_0\tanh(h/R)}{mR(1+\epsilon)} \tag{7.21}$$

and the new Berry frequency,

$$\Omega_B = \frac{4\pi e^2 \tanh(h/R)}{\hbar R(1+\epsilon)}\mathcal{F}, \tag{7.22}$$

we get for the bulk,

$$\begin{aligned} -\omega^2 N_j + \Omega_0^2 \frac{\Phi_{j+1}-\Phi_{j-1}}{2dx\cdot x_j} + \frac{l\Omega_B\omega}{4x_j}\left(\frac{\Phi_{j+1}}{x_{j+1}} + \frac{\Phi_j}{x_j} + \frac{\Phi_j}{x_j} + \frac{\Phi_{j-1}}{x_{j-1}}\right) \\ + \frac{\Omega_0^2}{dx^2}\left(\Phi_{j+1} - \Phi_j - \Phi_j + \Phi_{j-1}\right) + \frac{l\Omega_B\omega}{2dx}\left(\frac{\Phi_{j+1}}{x_{j+1}} - \frac{\Phi_{j-1}}{x_{j-1}}\right) \\ - \frac{l^2\Omega_0^2}{x_j^2}\Phi_j - \frac{l\Omega_B\omega}{x_j}\frac{\Phi_{j+1}-\Phi_{j-1}}{2dx} = 0, \end{aligned} \tag{7.23}$$

and for the edge,

$$\begin{aligned} -\omega^2 N_M + \Omega_0^2 \frac{\Phi_M - \Phi_{M-1}}{2dx\cdot x_M} + \frac{l\Omega_B\omega}{4x_M}\left(\frac{\Phi_M}{x_M} + \frac{\Phi_{M-1}}{x_{M-1}}\right) + \frac{\Omega_0^2}{dx^2}\left(-\Phi_M + \Phi_{M-1}\right) \\ + \frac{l\Omega_B\omega}{2dx}\left(-\frac{\Phi_M}{x_M} - \frac{\Phi_{M-1}}{x_{M-1}}\right) - \frac{\Omega_0^2 l^2}{x_M^2}\Phi_M - \frac{l\Omega_B\omega}{x_M}\left(\frac{\Phi_{M+1}-\Phi_{M-1}}{2dx}\right) = 0. \end{aligned} \tag{7.24}$$

We expect there to be no anomalous contribution in the bulk as mentioned earlier. It seems, however, that there *is* a contribution near the center where the appoximations made in the above chapters do not hold, in regions where $\frac{\Delta}{r_j} << 1$ is not true. To ease concerns over the legitimacy of the discretization we will below try to demonstrate what happens near the center of the disk.

We will focus solely on the terms that are proportional to Ω, and by extension, $\mathcal{F}$, in this part, so let us start by rewriting them as follows,

$$\begin{aligned} & c_\Omega\left[\frac{1}{4r_j}\left(\frac{\Phi_{j+1}}{r_{j+1}} + 2\frac{\Phi_j}{r_j} + \frac{\Phi_{j-1}}{r_{j-1}}\right) + \frac{1}{2\Delta}\left(\frac{\Phi_{j+1}}{r_{j+1}} - \frac{\Phi_{j+1}}{r_{j-1}}\right) - \frac{\Phi_{j+1}-\Phi_{j-1}}{2\Delta r_j}\right] \\ &= c_\Omega \frac{1}{r_j^2}\left[\frac{1}{4}\left(\frac{\Phi_{j+1}}{1+\frac{\Delta}{r_j}} + 2\Phi_j + \frac{\Phi_{j-1}}{1-\frac{\Delta}{r_j}}\right) + \frac{r_j}{2\Delta}\left(\frac{\Phi_{j+1}}{1+\frac{\Delta}{r_j}} - \frac{\Phi_{j+1}}{1-\frac{\Delta}{r_j}}\right) - \frac{r_j}{2\Delta}\left(\Phi_{j+1}-\Phi_{j-1}\right)\right], \end{aligned} \tag{7.25}$$

where $c_\Omega = \frac{n_0 e l\Omega}{\hbar}$ and we have used that $r_{j+1} - \Delta = r_j = r_{j-1} + \Delta$.
Due to the symmetry of the system the potential is always 0 at the center of the disk. It is connected to the two Bessel functions through equations (5.16) and (5.17) and (5.18). The Bessel functions at argument 0 go as l'th order polynomials, $J_l(x)|_{x\approx 0} \propto x^l$. This means that for large l the potential is essentially flat and equal to 0 near the center. The worst case scenario we could imagine is the one where the potential is linear near the center, $\Phi_j = Ar_j = A\Delta j$, for $j/M << 1$, which seems to happen for $l = 1$ based on the zero-field numerical results, see B.2. Let us now examine what happens for j=1 in this scenario. In this case potential near the center fulfills $\Phi_{j-1} = 0$ and, by assumption, approaches this value linearly, so that $\lim_{j\to 1}\frac{\Phi_{j-1}}{1-\frac{\Delta}{r_j}} = \lim_{j\to 1}\frac{A\Delta(j-1)}{1-\frac{1}{j}} = A\Delta = \Phi_1$ and $\Phi_2 = 2\Phi_1$. With these relations we can now write

$$c_\Omega \frac{1}{\Delta^2}\left[\frac{1}{4}\left(\frac{\Phi_2}{2}+2\Phi_1+\Phi_1\right)+\frac{1}{2}\left(\frac{\Phi_2}{2}-\Phi_1\right)-\frac{1}{2}\left(\Phi_2-0\right)\right] = c_\Omega \frac{1}{\Delta^2}\left[\Phi_1+\frac{1}{2}\left(\Phi_1-\Phi_1\right)-\Phi_1\right]=0, \tag{7.26}$$

which shows that there is no anomalous contribution at the center for $l = 1$. For larger l the potential is very flat and essentially zero near the center, and so providing no anomalous terms before the approximation starts to be applicable.

7.3 Numerical Results for the Anomalous Berry Plasmon

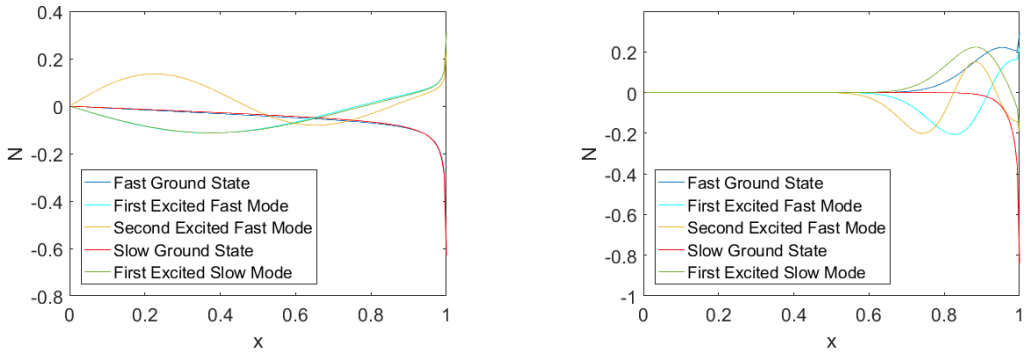

Figure 16: The density profiles of the first few Berry plasmon modes for $\mathcal{F} = 1$ and $l = 1$ (left)and $l = 30$ (right). The fast modes for $l = 30$ each have a "shoulder" that shows that it is merging with the bulk, ceasing to be an entirely confined edge mode.

When solving for the anomalous Berry plasmon modes using the discretization scheme outlined above we used a grid of $M = 160$ points to simulate our set of concentric circles. As a standard we will be using a disk of radius $R = 5 \cdot 10^{-6}$m, with unperturbed carrier density $n_0 = 10^{16}\text{m}^{-2}$, with vacuum above and below, so that $\epsilon = 1$, and with a plasmon mass $m = 0.03m_e$, with m_e being the electron mass. This allows us to find the eigenmodes and corresponding densities, yielding results similar to those of the magnetoplasmon case; we still see the confining effects of high angular momentum, the delocalizing (less confining to the edge) effect of exciting higher modes and the nodes that follow from excitations beyond the ground state. These features are displayed in figure 16 where the density profiles are shown for different excitations at angular momenta $l = 1$ and $l = 30$. New to the Berry plasmon is the advent of the merge between the fast edge mode and the bulk mode above a certain threshold, as predicted by Song and Rudner[11] for the infinite half-plane. By utilizing the local kernel approximation, they predict that the threshold frequency for the infinite half-plane is given by $\omega_{\text{threshold}} = \frac{\hbar n_0}{\sqrt{2m|\mathcal{F}|}}$, as found by setting the frequency of the mode equal to the bulk frequency for a given q. Using the physical quantities above, together with $\mathcal{F} = 1$, the threshold frequency becomes $\omega_{th} = 2.73 \cdot 10^{13}$Hz, which yields a corresponding angular momentum of around $l \approx 7$ when comparing this to the dispersion in figure 18a, where $\Omega_0 = 1.03 \cdot 10^{13}$Hz. This merging manifests itsef as the bump

in the density profile of the fast modes. It is especially evident in the density profile of the fast ground state mode; It has a peak before the edge of the disk and no longer behaves monotonically as it was wont to do before the merge.

Contrary to the case of the magnetoplasmons where the splitting was predicted to be constant (equations (4.11a)-(4.11b)) we see from figure 18a that the gap grows with the angular momentum and almost closes for low l ($l = 0$ has not been examined). This is to be expected as the anomalous terms never show up in equations (7.23) and (7.24) without a factor of l. The implicit dependence of the kernel on the angular momentum and that one term proportional to l^2 make the substitution of $\Omega_B l$ to some new variable impractical, but nevertheless the splitting rises almost linearly with l, see figure 24 in appendix B.1.

The modes are highly dependent on the amount of screening done by the plates, both in the absolute energy of the plasmon modes, but also in their dispersions. Figure 19 shows the evolution of the degenerate ground state mode for $\mathcal{F} = 0$ as the screening is varied. As the screening increases (h/R becomes smaller) the value of the lowest plasmon frequency increases in units of Ω_0, but decreases in absolute terms (note that Ω_0 scales with screening). This is indicative of the weakening of the electron long-range interaction. Below, in figure 17, we will see the manifestation of this in the wave-forms of these screened modes, with the caveat that this does not provide a full picture of the physics that would realistically be in play at this level of screening.
That the energy increases with the stiffness of the medium is a result that one might intuitively expect. Additionally, when the disk is fully screened and the interaction becomes local, the induced electric field between the concentrations of positively and negatively charged areas on the edge of the disk is quenched, and so the anomalous term, proportional to $\mathbf{E} \times \mathbf{\Omega}$, no longer causes either direction around the disk to be favoured, thereby killing the chirality of the modes as seen from the almost complete lack of splitting in figure 18b.

Furthermore, when the disk is subjected to full screening the particles behave like billiard balls, only exchanging momentum on impact. The linear dispersion of the fully screened (local) kernel can be explained through the following non-rigorous argument that begins with the combination of the continuity and Euler equations (equations (3.1) and (3.2)) in the zero-field, long wavelength limit,

$$\omega^2 n = -\frac{en_0}{m}\nabla^2\Phi. \tag{7.27}$$

In q-space, ∇^2 goes as q^2 while, in 2 dimensions, Φ goes like q^{-1}, as argued in chapter 4 right after equation (4.1). This leads to a dispersion that goes as a square root, $\omega \propto \sqrt{q}$. When the potential completely screened and becomes local in real space, being proportional $\delta(x - x')$, then it is constant in fourier space. This leads to a linear dispersion, $\omega \propto q$, as we see in figure

(18b). Experimental study of a screened plasmon system has been shown to yield a similar linear dispersion [12]. It is important to note than in this limit we ought to include the previously discarded pressure term containing s^2. Since it affects the dispersion linearly when there is no edge, as seen in equations (3.11) and (4.3) these two effects compete in this limit, whereas before, for small l or q, a square root evolution beat out a linear evolution for comparable prefactors. In this case the Coulomb interaction and the pressure term are on the same footing in the Euler equation, both being linear in n and go (at least in the absence of an edge) as q^2, so that the s-term will enter the dispersion through a modification to the slope. This can be seen by noting that, since the density and potential are directly proportional, we will get a term in the Euler equation of the form $-\left(\Omega_0^2 + \frac{s^2}{R^2}\right)\nabla^2 n$.

For purely demonstrative purposes, the wave-forms of these fully screened modes are shown in figure 17. These are just to show how changing the behaviour of the Coulomb interaction affects the density distribution and is not to be taken as quantitative results to be compared with others. To get these, $h/R = 0.0001$ was used for the bulk and Berry frequencies, as these would be killed off if we set $h/R = 0$ directly. On the other hand, an actual delta function was used as kernel to calculate the wave-forms. This is reasonable when $h/R << l^{-1}$, as it is in this case. To faithfully model an, at least slightly, realistic system, one should keep the pressure term as discussed. With this in mind, we see that, contrary to what we have seen previously, the maximal densities appear not on the edge, but in the bulk (with the exception of the groundstates of the $l = 1$). Furthermore, it is apparent that the charge pile-up on the edge, that we explicitly allowed through the boundary condition, seems to not happen when the Coulomb force is local. The explanation for this is probably two-fold: The first is an extension of the explanation for why the chiral splitting disappears for a fully screened Berry plasmon. When the Coulomb interaction is screened, then any displacement of charge is not felt by the surrounding charges and therefore no potential is induced. This means that there is no transverse current (the anomalous velocity is proportional to $\mathbf{E} \times \mathbf{\Omega}$) to push charge into the edge, which ought to alter the charge distribution near it. However, we still see charge pushed into the edge, even when we turn off any chirality-inducing field (see figures 25 and 26 in the appendix), so this cannot be the full reason. The second is that the electrons (charge elements) become "friendlier" to each other as the mutual repulsion is weakened, possibly making them less likely to push each other outward from the center.

7.4 Comparison of the Exact and Approximate Kernels

As we saw from figure 13a, and can see from figure 21, the correspondence between the dispersion for the disk and for the infinite half-plane is not astounding, even though there is a resemblance. To try to get a better agreement we will compare the disk dispersion with that of the infinite half-plane using the zero-field modes, numerically calculated with the exact kernel as given in equation 4.7 and equations (22a-b) of Fetter's first paper on the half-plane [4], where (the

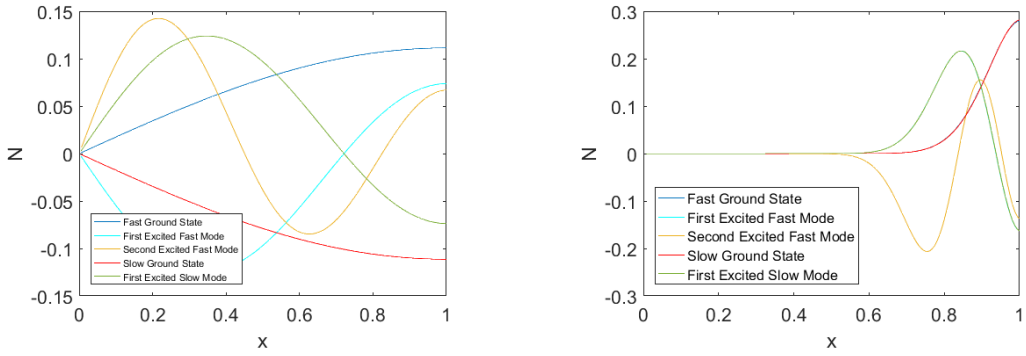

Figure 17: The density profiles of the first few fully screened Berry plasmon modes for $\mathcal{F} = 1$ and $l = 1$ (left)and $l = 30$ (right). Note that on the right the two ground states and the two first excited modes lie on top of each other.

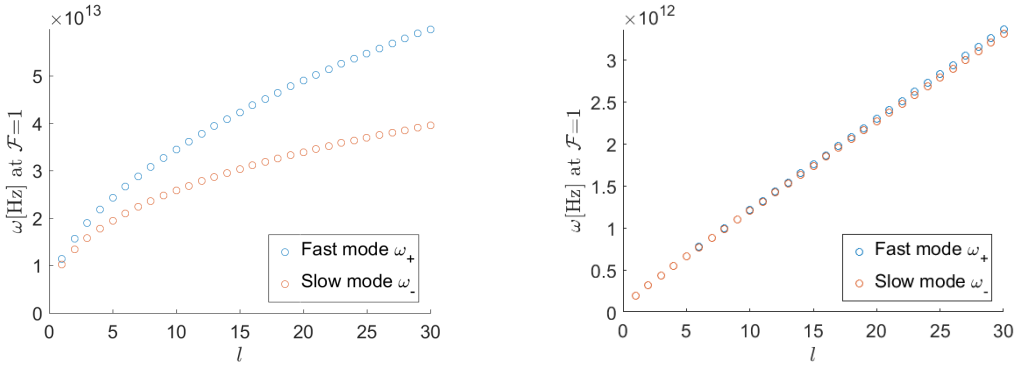

(a) The dispersion of the fast and slow ground state modes of the unscreened Berry plasmon. The splitting allows for determination of the unique counter-propagating modes.

(b) The dispersion of the fast and slow ground state modes of the fully screened ($\frac{h}{R} = 0.0001$) Berry plasmon. The splitting is likely due to the finite screening used.

Figure 18

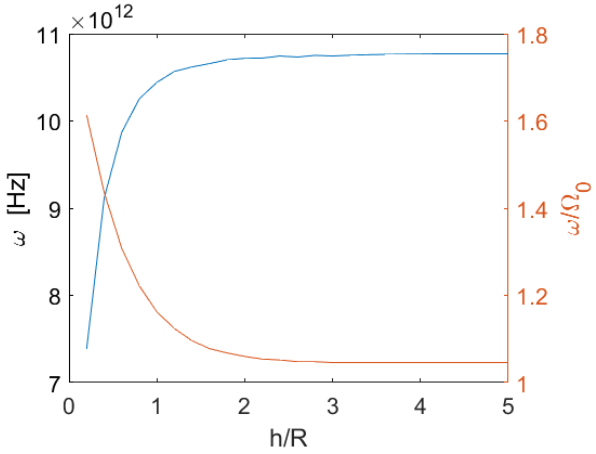

Figure 19: Value of the degenerate ground state modes for various amounts of screening in the no-field, no Berry flux case with $l = 1$. Note the offset of the second axis. The two graphs show the absolute frequency (blue) and the relative frequency as compared to the screening-dependent bulk frequency (orange).

medium lies in the negative half of the x-y-plane)

$$\Phi(x) = -4\pi e \int_{-\infty}^{0} dx'\, L(x - x')n(x') \tag{7.28a}$$

$$L(x) = \frac{1}{2}\int_{-\infty}^{\infty} \frac{dk}{2\pi} \frac{\mathrm{e}^{ikx}}{\sqrt{k^2 + q^2}} = \frac{1}{2\pi} K_0(q|x|), \tag{7.28b}$$

and using the same smearing procedure as detailed in chapter 6.2. Here we have renamed the kernel in the hopes of minimizing confusion with the Bessel function. The method of discretization is wholly analogous to that detailed in chapter 7.2 but in a half-plane geometry with translational invariance (up to a phase) along y (as counterpart to the angular direction), rather than a disk geometry. The plane will have a depth of a few disk radii to ensure that the edge modes have decayed properly to capture the full behaviour of the mode.

The resulting dispersion for $q \approx l/R$ corresponding to angular momenta $l = 1...30$ is plotted alongside the dispersion resulting from the approximated kernel and the disk plasmons, which utilize the exact kernel for that geometry, in figure 21, all for both $\mathcal{F} = 0$ and $\mathcal{F} = 1$. We see that the dispersion resulting from the exact kernel much more closely resembles the disk scenario when there is no net Berry flux, but that there is still a discrepancy when the Berry flux is added, the discrepancy being smaller for small angular momenta. This phenomenon is contrary to what one might have expected and further study is needed to determine the cause.

That the local kernel approximation results in lower energy modes, and the difference scaling with (anguar) momentum, can be explained directly through the shape of the local kernel potential; it sacrifices close range interaction strength for long-range interaction, essentially stretching and flattening the potential, see figure 20. This means that when we are in the long wavelength regime, where we have small l or q, the distance between the induced charge valleys and peaks is big and so the long range part of the interactions play the largest role. For

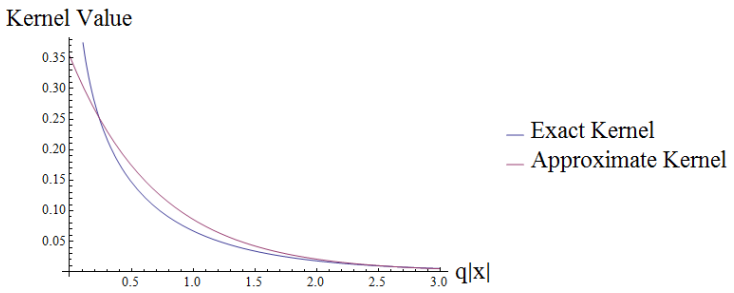

Figure 20: A graph of the two kernels for increasing argument, $q|x|$. We see that the kernels are vastly different for short-range interactions, indicating that they will lead to different dispersion behaviour as the momentum increases.

smaller wavelengths, corresponding to larger l or q, the short-range interaction plays a bigger and bigger role, and it is in this regime where the two kernels truly differ (as extreme as a diverging interaction versus a finite interaction for $q|x - x'| = 0$).

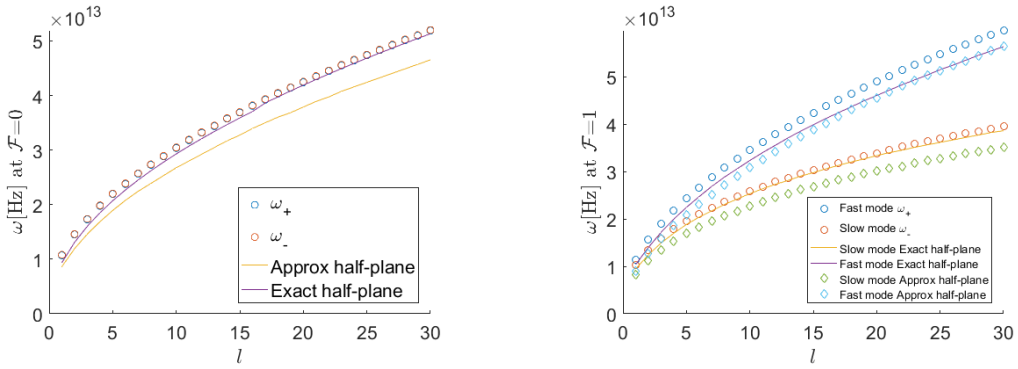

(a) Comparison of the dispersion of the degenerate ground states for the disk and the infinite half-plane with approximate and exact kernel, respectively.

(b) Comparison of the dispersion of the now split ground states for the disk and the infinite half-plane with approximate and exact kernel, respectively, for $\mathcal{F} = 1$. This has a discrepancy still, but it is improved compared to the dispersion resulting from the approximate kernel.

Figure 21: A comparison of the dispersions of the disk and the infinite half-plane. Circles indicate the quantized nature of the disk dispersion while solid lines refer to the continuous half-plane dispersions.

7.5 Edge Modes in Insulator Disk

In a regular 2-band conductor with a partially filled conductance band, $\mathcal{F} = 1$ will not usually be possible because the Berry curvature of different bands cancel, because, as we recall from chapter 2.1, the sum of the Berry curvature over all bands vanishes, $\sum_n \Omega^n_{\mu\nu} = 0$, so in a 2-band system any particles excited to the conduction band will cancel some of the contribution from the valence band. In an insulator, where the chemical potential is placed in the band gap and

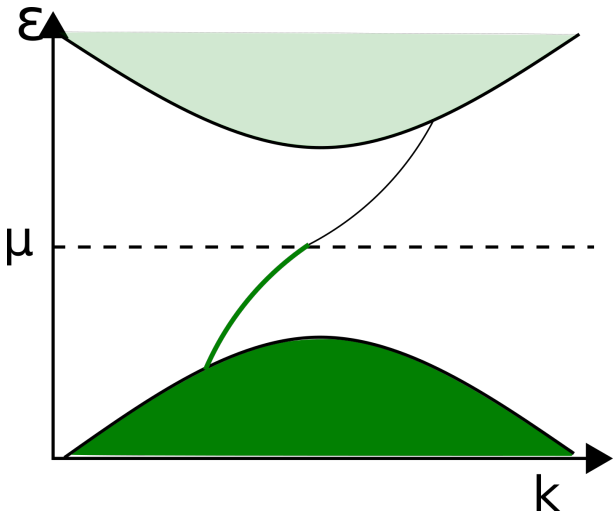

Figure 22: An illustration of a set of edge states connecting the valence and conduction bands in a 1D insulator, where dark green indicates filled states and pale green indicates vacant states. The derivative of the energy w.r.t. the wave vector, **k**,is positive on average, so that the group velocity is positive, leading to an edge current.

the conduction band is empty, we can have $\mathcal{F} = 1$. In this case, however, there are no free charge carriers which means that $n_0 = 0 \Rightarrow \Omega_0 = 0$, and so it is safe to assume that there is no density perturbation in the bulk and, by extension, no induced electromagnetic potential. When the bulk potential is zero then the approximation made in equation (7.18) holds. Using this on equation (7.23) kills all the terms proportional to $\mathcal{F}$ in the bulk and $n_0 = 0$ kills the remaining terms such that

$$-\omega N_j = 0, \tag{7.29}$$

which means that there will be no density perturbation in the bulk. On the edge of the disk (which is governed by equation (7.24)), with the boundary condition that allows charge to pile up, but not flow out of the disc, we get terms that survive. These terms allow for a mode that is localized on the edge. The need for the existence of these edge modes can be explained by considering a two-dimensional slab of insulating crystal, infinite in the x-direction and finite in the y-direction, with non-zero Berry curvature. The non-zero Berry curvature means that an electric field applied along the x-direction, while unable to accelerate the inert electrons in the valence band of the insulator, will cause a current to run in the y-direction (see equation (2.36)), thereby causing charges to pile up on the edge. The particles on the edge all have a velocity close to the "Fermi velocity", $\frac{\partial \epsilon_n(\mathbf{k})}{\hbar \partial \mathbf{k}} \approx v_F$, and so a current runs along the edge, see figure 22.

An alternative argument posed in [17] illustrates the need for such an edge mode by considering the case where two topological insulators with differing Chern numbers are placed next to each other. If the Chern number, and through equation 2.40, the anomalous Hall conductivity, cannot be changed without closing the insulating gap, then there MUST be a gap-closing, and subsequent reopening to regain the insulating properties, on the intersection between the two

topologically different and non-trivial (non-zero Chern number) areas.

We expect such an edge state that will host plasmon excitations to exist in the disk geometry. An electric field, applied or induced, in the radial direction will cause the disk to have a current running around the edge, while one applied in the angular direction will force charge into, or out of, the edge. Exciting an edge plasmon in this case will have it living alongside the edge current of the insulator, as proposed above. This current will give a boost to the propagation velocity of the anomalous edge Berry plasmon but we will have to manually assign a velocity, $v_{edge} \approx v_F$, where v_F is the Fermi velocity, to these edge states. Since the edge velocity is constant and $n_0 = 0$ we will merely have an (uncharged) density current $j_\theta = nv_{edge}$. This we will add to $\overline{v}_\theta$ in the continuity equation, (7.4), and with

$$\frac{\partial}{\partial\theta} j_\theta = \left(\frac{\partial}{\partial\theta} n\right) v_{edge} = ilnv_{edge} \tag{7.30}$$

and the discretization scheme and definitions above, we get a final equation to be solved for the edge mode,

$$-\omega N_M + \frac{l\Omega_B}{4x_M}\left(\frac{\Phi_M}{x_M} + \frac{\Phi_{M-1}}{x_{M-1}}\right) - \frac{l\Omega_B}{2dx}\left(\frac{\Phi_M}{x_M} + \frac{\Phi_{M-1}}{x_{M-1}}\right) - \frac{l\Omega_B}{x_M}\left(\frac{\Phi_{M+1} - \Phi_{M-1}}{2dx}\right) + \frac{lv_{edge}}{x_M R} N_M = 0, \tag{7.31}$$

which is just equation (7.24) with $\Omega_0 = 0$ and the new term added after dividing through by ω. $x_M = 1$ but we have written it explicitly for ease of comparison. Here we could follow the tradition of hiding the factors of R in frequencies, so let us define a new frequency, $\Omega_{edge} = \frac{v_{edge}}{R}$. Since equation (7.31) is linear in ω we can see that we will only get one solution (together with the $\omega = 0$ solution) and so only one mode survives. This is the unidirectional plus mode that makes this system seemingly fit for the role of a circulator as discussed in chapter 1. This is not entirely unexpected as decreasing Ω_0 (through n_0) is decreasing the parts that the fast and slow modes have in commmon, while leaving the splitting be.

By making the substitution $\omega' = \omega - l\Omega_{edge}$ we get the exact same equation but without the added term, and so we see that ω' is just the original mode with a boost proportional to the speed (the sign determines the direction) of the individual electrons at the edge of the disk.

The resulting dispersion is seen in figure 23a. Notably the dispersion tends more toward being linear than that of the conductor and reminiscent of the dispersion of the fully screened disk, as seen in figure 18b. This is likely because the bulk of the disk is effectively fully screened by the presence of the postive background, so that the charge on the edge only sees the charge elsewhere on the edge, reminiscent of a plasmon in 1 dimension, which has a linear dispersion [18].

On the other hand, when one allows for the edge velocity to be present in the regular conductor (figure 23b) then the effect is hardly noticeable, as $\frac{\Omega_{edge}}{\Omega 0} \approx 10^{-3}$.

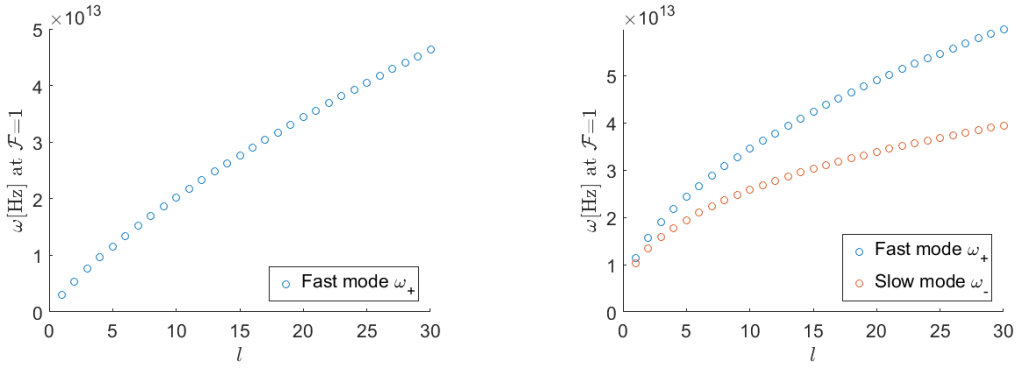

(a) (b)

Figure 23: The dispersion for (a) the lone unidirectional edge mode of the topological insulator ($n_0 = 0$) and (b) the split modes of the conductor, ($n_0 = 10^{16}\mathrm{m}^{-2} = 10^{12}\mathrm{cm}^{-2}$), both with an edge velocity $v_{edge} = 10^5 \frac{\mathrm{m}}{\mathrm{s}}$.

8 Conclusion

The case of the bulk and surface (magneto-)plasmons in 3D is well known and the underlying physics understood. When delving into the physics of 2D systems an analytical solution for the dispersion requires an approximation of the Coulomb interaction; an approximation which we have seen to consistently underestimate the energy/frequency of the modes. Edge plasmons in 2D systems can acquire a chiral energy splitting through the application of an external magnetic field or through the use of a material with non-vanishing Berry curvature. Such a splitting, with tunable resonances in the case of magnetoplasmons, has the potential to be useful in applications such as circulators and its derivative devices.

Using the concentric ring discretization scheme allowed for a numerical solution for the (chiral) modes and wave-forms of edge plasmons on the disk. For example, the zero-field 2D mode was predicted in chapter 4 to grow as $\omega_\pm = \pm\sqrt{2l/3}\Omega_0$, whereas numerical calculation with the exact kernel, as given in equation (5.18), leads to a dispersion that grows faster than that, as we saw from figure 13a. When the curvature of the edge of the disk is small on the scale of a full wavelength, then it is possible to make comparisons to the results for the infinite half-plane, often solved with the local kernel approximation. Such a comparison reveals that the local kernel approximation fundamentally changes the electron interactions, especially for large (angular) momentum. Numerical computation of the half-plane system with the exact Coulomb interaction made the dispersion in the two situations much more comparable, although work is still needed to see the similarity in the chiral splitting of the modes.

We saw in chapters 6.4 and 7.3 that for both magneto- and Berry plasmons that the confinement to the edge of the edge modes increased with angular momentum while higher excited modes stretched further into the bulk than low excitations. Additionally, higher excitations come with a node for every excitation above the ground state. Above a certain threshold in angular momentum, we start to see the fast mode of the Berry plasmon seeping into the bulk through a

hump in the wave-form of the density perturbation. The behaviour of the plasmons depends strongly on the induced potential. Weakening the long-range interactions of the electrostatic potential via screening plates causes a lowering of the frequency of the modes and makes the dispersion linear when the interaction is fully screened. In such a situation we can no longer claim to be in the long wavelength limit and extra precautions have to be taken.
Non-vanishing Berry curvature affects the behaviour of plasmons only on the edge of the medium, causing a splitting which grows (almost linearly) with angular momentum, as contrary to magnetoplasmons whose splitting is (near) constant. Finally, we detailed how this leads to the fact that the fast mode exists even when the bulk of the medium is an insulator, i.e. when the charge carrier density, n_0, is set to 0, and how the resulting system can be seen to have only one surviving unidirectional mode.

The possibilities of further study are numerous. An immediate extension of the presented work would be to examine the various cases with intermediate, non-extreme screening and to find the reason for the mismatch between half-plane and disk results for high angular momentum for the chiral Berry modes. The reaction of the plasmon mode to a probing electric field would increase the usability of theoretical predictions in comparisons with those of experiments, as would keeping the finite lifetime of the mode to better model a realistic scenario, and so this is worth considering implementing. An alternative pursuit would be to more closely try to model the circulator theoretically. Recent experimental studies that realize and study the nonreciprocity of both the magnetoplasmon and chiral Berry plasmon circulators, [2][3], allow for comparison with theoretically predicted results.

A Edge Magnetoplasmons in Disk Geometry

In [6] Fetter examines the edge magnetoplasmons on a disk of finite radius. He does this, however, with the method of restricting the flow into the edge of the disk and thereby potentially throttling the transverse part of the current caused by the presence of the magnetic field; current which would otherwise flow around the perimeter of the disk, $j_\theta\,|_{r=R}$, gets a radial component due to the Lorentz force. Without edge states this charge has nowhere to go and so it seems an unrealistic boundary condition.

In this chapter we will try to combine the works of Fetter in his two articles, [5] and [6], to impose the condition of a finite edge flow onto the magnetoplasmon problem in disk geometry and reach an analytical expression to be solved for the allowed frequencies and their density distributions. There will be many straightforward parallels and therefore, unless otherwise is stated, all references to outside equations are to the equations in [5].

A.1 Analytical Eigenvalue Equation

In this chapter we will derive an analytical equation to determine the modes of the disk magnetoplasmons. The disk will have radius R, rest on a material with dielectric constant ϵ, with vacuum ($\epsilon_{vacuum} = 1$) above it. We will again be looking for steady state solutions and utilize the rotational symmetry of the system to simplify time and angular derivatives.

We start out with the usual fluid equations governing our material in cylindrical coordinates,

$$-i\omega n + n_0 \nabla \cdot \mathbf{v} = 0 \tag{A.1}$$

$$-i\omega \mathbf{v} + \frac{s^2}{n_0}\nabla n - \frac{e}{m}\nabla \Phi|_{z=0} - \omega_c \hat{z} \times \mathbf{v} = 0. \tag{A.2}$$

In cylindrical coordinates we have (though we only consider the polar parts in the plane of the disk)

$$\mathbf{v} = \begin{pmatrix} v_r \\ v_\theta \end{pmatrix}, \tag{A.3}$$

$$\hat{z} \times \mathbf{v} = \begin{pmatrix} -v_\theta \\ v_r \end{pmatrix}, \tag{A.4}$$

and

$$\nabla = \begin{pmatrix} \partial_r \\ \frac{\partial_\theta}{r} \end{pmatrix}. \tag{A.5}$$

We can now consider the first and second components of this vector equation seperately. For the first component we get

$$i\omega v_r + \partial_r \left(\frac{e}{m}\Phi - \frac{s^2}{n_0} n \right) - \omega_c v_\theta = 0 \Leftrightarrow v_\theta = \frac{1}{\omega_c} \left(i\omega v_r + \partial_r \left(\frac{e}{m}\Phi - \frac{s^2}{n_0} n \right) \right), \tag{A.6}$$

and from the second component we get

$$\begin{aligned} &i\omega v_\theta + \frac{1}{r}\partial_\theta \left(\frac{e}{m}\Phi - \frac{s^2}{n_0} n \right) + \omega_c v_r = i \left(\frac{\omega}{\omega_c}\partial_r + \frac{l}{r} \right) \left(\frac{e}{m}\Phi - \frac{s^2}{n_0} n \right) - \frac{\omega^2}{\omega_c} v_r + \omega_c v_r = 0 \\ \Leftrightarrow &i \left[\omega \partial_r + \frac{l\omega_c}{r} \right] \left(\frac{e}{m}\Phi - \frac{s^2}{n_0} n \right) + \left(\omega_c^2 - \omega^2 \right) v_r = 0. \end{aligned} \tag{A.7}$$

We will now change variables to $x = \frac{r}{R}$, $L = |l|$ and $\Omega_c = |\omega_c|$.

$$i \left[\frac{\omega}{R}\partial_x + \frac{L\Omega_c}{xR} \right] \left(\frac{e}{m}\Phi - \frac{s^2}{n_0} n \right) + \left(\Omega_c^2 - \omega^2 \right) v_r = 0. \tag{A.8}$$

Rather than setting $v_r = 0$ at the boundary we will instead make use of the boundary condition that the current into the boundary is the change in density on the edge, so for $x = 1^-$ we have $-en_0 v_r = -e\partial_t n^* = ei\omega n^*$ such that $v_r = -i\omega \frac{n^*}{n_0}$. Let us evaluate (A.8) at $x = 1^-$ to use this boundary condition,

$$\begin{aligned} i\left[\frac{\omega}{R}\partial_x + \frac{L\Omega_c}{xR}\right]\left(\frac{e}{m}\Phi - \frac{s^2}{n_0}n\right)\Big|_{x=1^-} + i\left(\omega^2 - \Omega_c^2\right)\omega\frac{n^*}{n_0} = 0 \\ \Leftrightarrow \left[\partial_x + \frac{L\Omega_c}{\omega}\right]\left(\frac{en_0}{m}\Phi - s^2 n\right)\Big|_{x=1^-} = \left(\Omega_c^2 - \omega^2\right)Rn^* \end{aligned} . \tag{A.9}$$

Now we can multiply both sides by $\frac{4\pi e\tanh(\frac{h}{R})}{R(1+\epsilon)}$ to get

$$\left[\partial_x + \frac{L\Omega_c}{\omega}\right]\left(\Omega_0^2\Phi - \frac{s^2}{R^2}N\right)\Big|_{x=1^-} = \left(\Omega_c^2 - \omega^2\right)N^*, \tag{A.10}$$

where

$$\begin{aligned} \Omega_0^2 &= \frac{4\pi n_0 e^2\tanh(\frac{h}{R})}{mR(1+\epsilon)} \\ N(x) &= \frac{4\pi eR\tanh(\frac{h}{R})}{1+\epsilon}n(x) \\ N^* &= \frac{4\pi e\tanh(\frac{h}{R})}{1+\epsilon}n^*. \end{aligned} \tag{A.11}$$

Here there are quite clear parallels to equations (6a-b), (9b), (10a) in [5] with the substitution $q \sim \frac{1}{R}$. Equation (A.10) above is the new boundary equation that is to replace equation (12) in [6]. The bulk equation is found as before by combining the continuity equation, (A.1), with the Euler equation, (A.2), using (3.8) and expressing everything in terms of (A.11), which gives

$$\left[\frac{1}{x}\partial_x x\partial_x - \frac{L^2}{x^2}\right]\left[\Omega_0^2\Phi - \frac{s^2}{R^2}N\right] = -\left(\Omega_c^2 - \omega^2\right)N. \tag{A.12}$$

We will make use of the same Green's functions as used in [6] that obey the conditions

$$\left[\frac{1}{x}\partial_x x\partial_x - \frac{L^2}{x^2}\right]G(x,x') = -\frac{1}{x}\delta(x-x'), \tag{A.13}$$

and

$$\left[\partial_x + \frac{L\Omega_c}{\omega}\right]G(x,x')\big|_{x=1^-} = 0, \tag{A.14}$$

which is fulfilled for

$$G(x,x') = \frac{\omega - \Omega_c}{\omega + \Omega_c}\gamma(x,x') + g(x,x'), \tag{A.15}$$

where

$$\begin{aligned} \gamma(x,x') &= \frac{1}{2L}(xx')^L \\ g(x,x') &= \frac{1}{2L}\frac{x_<}{x_>} \end{aligned} \tag{A.16}$$

and $x_<$ and $x_>$ are the smaller and larger of x and x' respectively.

With these Green's functions we can use equation (A.13) to rewrite equation (A.12),

$$\left[\frac{1}{x}\partial_x x\partial_x - \frac{L^2}{x^2}\right]\left[\Omega_0^2\Phi - \frac{s^2}{R^2}N\right] = \left(\Omega_c^2 - \omega^2\right)\int_0^1 dx'x'\left[\frac{1}{x}\partial_x x\partial_x - \frac{L^2}{x^2}\right]G(x,x')N(x'). \quad \text{(A.17)}$$

This must mean that if we integrate out the operators the functions operated on must differ only up to a function that itself is the solution to

$$\left[\frac{1}{x}\partial_x x\partial_x - \frac{L^2}{x^2}\right]h(x) = 0. \quad \text{(A.18)}$$

The correct term is calculated in appendix A.2 and the full expression becomes

$$\left[\Omega_0^2\Phi - \frac{s^2}{R^2}N\right] = \left(\Omega_c^2 - \omega^2\right)\int_0^1 dx'x'G(x,x')N(x') + \left(\Omega_c^2 - \omega^2\right)G(x,1)N^*, \quad \text{(A.19)}$$

which has a straight parallel to equation (18) in [5] if we substitute the new term using the new boundary equation, equation (A.10) above. To take into account the charge on the edge and its effect on the whole disk the potential gets an additional term,

$$\Phi(x) = -\int_0^1 K(x,x')x'N(x') \to -\int_0^1 K(x,x')x'N(x') - K(x,1)N^*. \quad \text{(A.20)}$$

From here we can collect all terms on one side, insert $G(x,x)$ and $\Phi(x)$ on their respective spots to get the equation to be solved,

$$\begin{aligned}&\frac{s^2}{R^2}N + \Omega_0^2\int_0^1 dx'x'K(x,x')N(x') - (\omega-\Omega_c)^2\int_0^1\gamma(x,x')N(x') - \left(\omega^2-\Omega_c^2\right)\int_0^1 dx'x'g(x,x')N(x')\\ &+\left[\Omega_0^2K(x,1) - (\omega-\Omega_c)^2\gamma(x,1) - \left(\omega^2-\Omega_c^2\right)g(x,1)\right]N^* = 0,\end{aligned} \quad \text{(A.21)}$$

where the term in parenthesis is the new contribution from the edge. The rest is exactly like equation (22) from [6].

This is the equation that must be solved to determine the allowed modes and their corresponding radial density distributions. The most natural way to solve such an equation that, in most cases, does not have an analytical answer is to discretize would be to solve this numerically. Unfortunately this method seemingly provides no way to determine N^*, nor do most numerical approaches deal well with delta functions. It is for that reason that we have attempted to discretize the system from an earlier point and apply the boundary condition to the discretized system.

A.2 Calculating the Additional Term in Equation (A.19)

Here we show how to get to equation (A.19) from

$$\left[\frac{1}{x}\partial_x x\partial_x - \frac{L^2}{x^2}\right]\left[\Omega_0^2\Phi - \frac{s^2}{R^2}N\right] = \left(\Omega_c^2 - \omega^2\right)\int_0^1 dx'x'\left[\frac{1}{x}\partial_x x\partial_x - \frac{L^2}{x^2}\right]G(x,x')N(x'), \quad \text{(A.22)}$$

by integrating out the operator on both sides.

The two functions can differ up to a term that obeys

$$\left[\frac{1}{x}\partial_x x\partial_x - \frac{L^2}{x^2}\right] h(x) = 0. \tag{A.23}$$

This is the Euler-Cauchy equation. One solution can be found by inserting a power law trial function, x^m, which gives the equation $(m^2 - L^2)x^{m-2} = 0 \Leftrightarrow m = \pm L$, so that

$$h(x) = Ax^L + Bx^{-L} \tag{A.24}$$

is a solution. Now, we want our potential and densities to be bounded, so the B-term will have to go to avoid blowing up at the center of the disk, at x=0. This leaves us with $h(x) = Ax^L$. To find A we will now apply the operator $\partial_x + \frac{L\Omega_c}{\omega}$ to both sides of equation (A.22) and invoke our two boundary equations, equations (A.10) and (A.14), which means we must have

$$\begin{aligned}\left[\partial_x + \frac{L\Omega_c}{\omega}\right] Ax^L\big|_{x=1^-} &= \left(\Omega_c^2 - \omega^2\right) N^* \\ \Leftrightarrow A &= \left(\frac{1}{L}\frac{1}{1+\frac{\Omega_c}{\omega}}\right)\left[\Omega_c^2 - \omega^2\right] N^*.\end{aligned} \tag{A.25}$$

The function that we we have left in equation (A.22) is then Ax^L. We can rewrite the term in parenthesis in the expression for A to get

$$A = \frac{1}{2L}\left(\frac{\omega - \Omega_c}{\omega + \Omega_c} + 1\right)\left[\Omega_c^2 - \omega^2\right] N^*, \tag{A.26}$$

such that we can finally write the revised equation (A.22),

$$\begin{aligned}&\left[\Omega_0^2\Phi - \frac{s^2}{R^2}N\right] - \left(\Omega_c^2 - \omega^2\right)\int_0^1 dx' x' G(x,x')N(x') = Ax^L \\ &= \frac{1}{2L}\left(\frac{\omega - \Omega_c}{\omega + \Omega_c} + 1\right) x^L\left[\Omega_c^2 - \omega^2\right] N^*.\end{aligned} \tag{A.27}$$

The term on the RHS is exactly the edge-term in equation (A.19),

$$\begin{aligned}G(x,1)\left[\left(\partial_x + \frac{L\Omega_c}{\omega}\right)\left[\Omega_0^2\Phi - \frac{s^2}{R^2}N\right]\right]\Big|_{x=1^-} &= G(x,1)\left[\Omega_c^2 - \omega^2\right] N^* \\ = \frac{1}{2L}\left(\frac{\omega - \Omega_c}{\omega + \Omega_c} + 1\right) x^L\left[\Omega_c^2 - \omega^2\right] N^*,\end{aligned} \tag{A.28}$$

which can be seen by direct insertion of the form of $G(x,x')$.

B Auxillary plots

B.1 The Splitting of Berry Modes

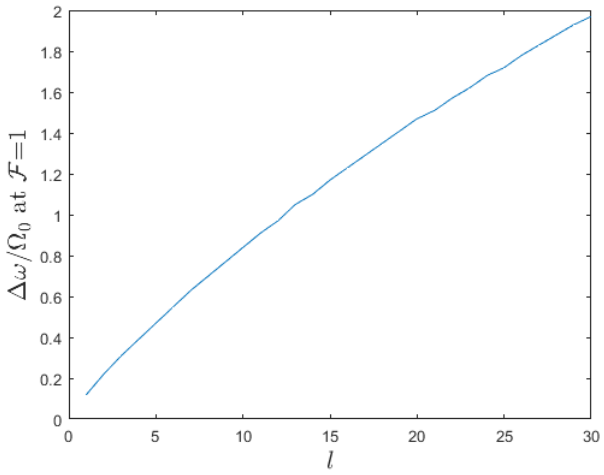

Figure 24: The splitting of the chiral Berry plasmon modes, $\Delta\omega = |\omega_+| - |\omega_-|$ in units of the bulk frequency, Ω_0. The splitting is almost linear. The deviation is likely due to the Coulomb kernel's dependence on angular momentum, l, but not the Berry curvature, Ω.

B.2 Zero-Field Wave-Forms

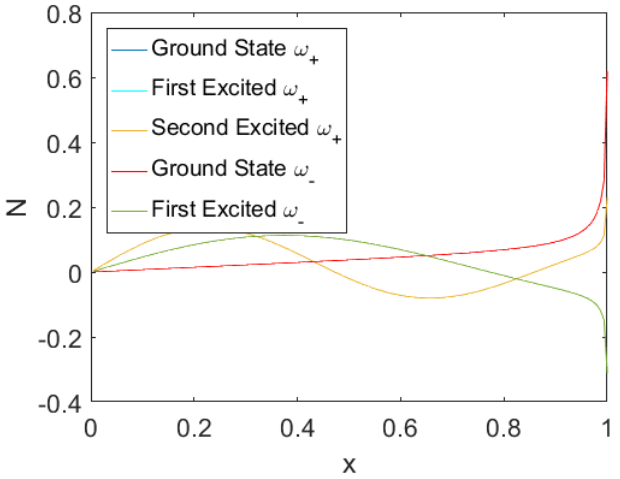

Figure 25: The wave-form of the first few zero-field modes for $l = 1$. Note that in the zero-field case the modes are completely degenerate and only differ in their angular dependence, $\pm l$, and so the negative and positive modes overlap completely.

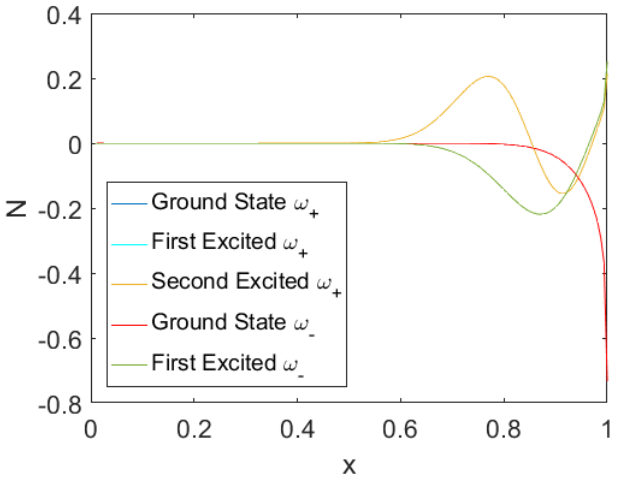

Figure 26: The wave-form of the first few zero-field modes for $l = 30$. Note that in the zero-field case the modes are completely degenerate and only differ in their angular dependence, $\pm l$, and so the negative and positive modes overlap completely.

References

[1] Viola, G. and DiVincenzo, P., *Hall Effect Gyrators and Circulators*, Phys. Rev X **4**, 021019 (2014).

[2] Mahoney, Colless et al., *On-Chip Microwave Quantum Hall Circulator*, Phys. Rev X **7**, 011007 (2017).

[3] Mahoney, Colless et al., *Zero-Field Edge Magnetoplasmons in a Magnetic Topological Insulator*, ArXiv e-prints, 1703.03122 (2017).

[4] Fetter, Phys. Rev. B, vol 32, No. 12, (1985).

[5] Fetter, Phys Rev. B, vol 33, No. 6, (1986).

[6] Fetter, Phys. Rev. B, vol. 33, No. 8, (1986).

[7] Ritchie, R. H., Phys. Rev. 106, 874 (1957).

[8] Xiao, Chang, Niu, Rev. Mod. Phys., Vol. 82, No. 3, (2010).

[9] Born, M. and Fock, V., *Beweis des Adiabatensatzes*, Zeitschrift für Physik A, (1928).

[10] Kato, T, J Phys. Soc. Jpn. **5**, 435, (1950).

[11] Song, Justin and Rudner, Mark, *Chiral plasmons without magnetic field*, PNAS vol. **113**, no. 17, (2016).

[12] Pablo Alonso-Gonzalez et al. Nature Nano, Vol 12, 31, (2017)

[13] Hasan, M. and Kane, C., *Colloquium: Topological Insulators*, Rev. Mod. Phys., Vol 82, (2010).

[14] Bernevig, B., Hughes, T., and Zhang, S., *Quantum Spin Hall Effect and Topological Phase Transition in HgTe Quantum Wells*, Science, Vol 314 (2006).

[15] Qi, X., Hughes, T., and Zhang, S., Topological Field Theory of Time-Reversal Invariant Insulator Phys. Rev. B **78**, (2008).

[16] Haldane, F. D. M., *Model for a Quantum Hall Effect without Landau Levels: Condensed-Matter Realization of the "Parity Anomaly", Am.Phys.Soc, Vol 61, no. 18, (1987).*

[17] Bernevig, B., *Topological Insulators and Topological Superconductors*, Princeton University Press, (2013)

[18] Bruus, H., and Flensberg, K., *Many-Body Quantum Theory in Condensed Matter Physics*, Oxford Graduate Texts, (2004).